

The geometry of state-space in plane Couette flow

By **J. F. GIBSON, J. HALCROW, AND P. CVITANOVIĆ**

School of Physics, Georgia Institute of Technology, Atlanta, GA 30332, USA

(Printed 27 May 2007)

Motivated by recent detailed experimental and numerical studies of recurrent coherent states observed in boundary shear flows, we initiate a systematic exploration of the hierarchy of exact unstable invariant solutions of the Navier-Stokes equations. We construct a dynamical, 10^5 -dimensional state-space representation of plane Couette flow at $Re = 400$ in a small, periodic cell and offer a new visualization of invariant manifolds embedded in such high-dimensional state-spaces. We compute the leading linearized stability exponents and eigenfunctions of known steady states at this Re and cell size. What emerges from global continuations of their unstable manifolds is a surprisingly simple and elegant dynamical-systems visualization of moderate Re turbulence. The invariant manifolds tessellate the region of state-space explored by transiently turbulent dynamics with a rigid web of continuous and discrete symmetry-induced heteroclinic connections.

1. Introduction

In a seminal paper, Hopf (1948) visualized the function space of Navier-Stokes velocity fields as an infinite-dimensional state-space, parameterized by viscosity, boundary conditions and external forces, with the instantaneous state of a flow represented by a point in state-space. Laminar states correspond to steady state points, globally stable for sufficiently large viscosity. As the viscosity decreases (as the Reynolds number increases), turbulent states set in, represented by chaotic state-space trajectories. Hopf's observation that viscosity causes a contraction of state-space volumes under the action of dynamics led to his key conjecture: that long-term, typically observed solutions of the Navier-Stokes equations lie on finite-dimensional manifolds embedded in the infinite-dimensional state-space of allowed states. These manifolds, known today as 'inertial manifolds,' are well-studied in the mathematics of spatio-temporal PDEs. Their finite dimensionality for non-vanishing viscosity parameters has been rigorously established in certain settings by Foias *et al.* (1985) and collaborators.

The concept of coherent states in turbulent flows is supported by a great deal of experimental and numerical evidence. Many unstable steady states, traveling waves, periodic orbit and relative periodic orbit solutions of canonical shear flows have been observed both in experiments and numerical simulation. These discoveries (described below in §2) open a new way of thinking about 'recurrent coherent states' in wall-bounded turbulent shear flows.

The long-term goals of this research program are to develop a dynamical systems description of moderate- Re turbulence based on exact unstable invariant solutions of the Navier-Stokes equation, to describe turbulent dynamics quantitatively as a walk through a set of unstable invariant solutions, and to apply this to the calculation of turbulent transport averages and control of boundary shear turbulence. Working toward these goals in the context of plane Couette flow, we describe how to (a) represent Navier-Stokes as a dynamical system, (b) determine/verify steady state solutions of Navier-

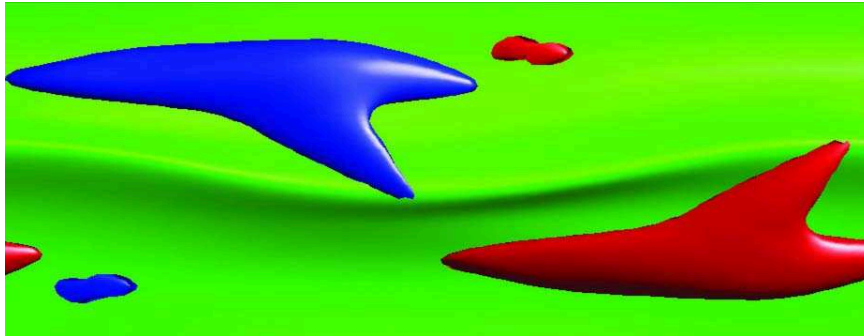


FIGURE 1. Streaks and staggered quasi-streamwise vortices in plane Poiseuille flow, $\alpha = 0.5, \gamma = 1.3, Re_{sn} \approx 244$. Waleffe (2003), figure 15. For a discussion, see § 2.

Stokes, (c) compute their linearized eigenvalues and eigenvectors, and (d) compute their unstable manifolds, and their homo/heteroclinic connections.

The point of departure for the exploration of the Navier-Stokes state-space undertaken here are the 3D unstable steady state and traveling wave ‘exact coherent states’ computed by Waleffe (2003). By “exact,” we mean a fully-resolved numerical solution of Navier-Stokes, as opposed to a solution of a model of Navier-Stokes. Most simulations in this paper are resolved to single-precision accuracy. While we do explore the boundary between laminar attractor and turbulence, our primary goal is to understand the strongly turbulent regions of state-space rather than the laminar state threshold perturbation needed to reach turbulence. In this paper, we recast a canonical Navier-Stokes turbulent shear flow, plane Couette flow, as a dynamical system in a high-dimensional state-space, of order of 10^4 - 10^5 . We make no modeling assumptions or approximations; all our calculations are fully-resolved direct numerical simulations of the Navier-Stokes equations.

In numerical fluid dynamics, simulations are commonly visualized as time-varying velocity and vorticity fields in 3D physical space, such as figure 1. Such a visualization, of which figure 1 is one frame in a time sequence, is invaluable for developing intuition about the physical origin of the recurrent coherent states in wall-bounded turbulent shear flows (Waleffe (1998)).

The key new tool developed here is an alternative, dynamical systems visualization of the Hopf’s state-space; for moderate Re flows, our projections from 10^4 - 10^5 dimensional state-space to a 3-dimensional frame offer a complementary and often informative viewpoint. For example, in figure 2 unstable steady states are points, but the geometry of their unstable manifolds and their interconnections offer insights into turbulent dynamics that would be hard to glean from the 3D configuration space time-dependent snapshots of the flow. How such state-space portraits are constructed is explained in § 6.

We review the experimental and computational evidence for recurrent coherent states in § 2 and describe plane Couette flow in § 3. The CFD algorithm employed and our dynamical state-space representation of Navier-Stokes flows is described in § 4, with tabulation of numerical results relegated to appendix § B. The computation of steady states and their linear stability eigenvalues and eigenfunctions is described in § 5. As searches for exponentially unstable recurrent coherent states require highly accurate, reliable computational methods, sections § 2 to § 5 and appendix § A are technical in nature out of necessity.

They set the stage for the main advance reported in this paper, visualization and exploration of the state-space of moderate Re plane Couette flow undertaken in § 6. The

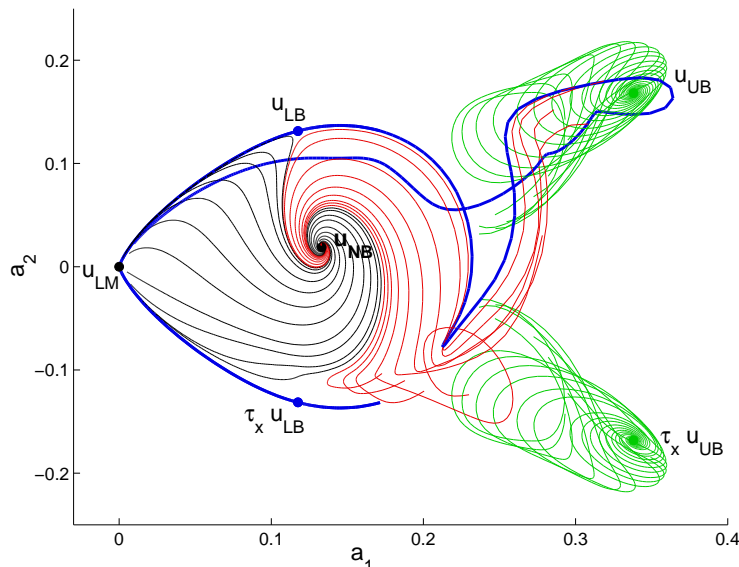


FIGURE 2. A state-space portrait of plane Couette flow for $Re = 400$ and $[L_x, L_y, L_z] = [2\pi/1.14, 2, 4\pi/5]$ cell, projection from 61,506 dimensions to 2. The labeled points are exact steady states (equilibrium solutions) of the Navier-Stokes equation; the curved trajectories are fully-resolved numerical integrations of Navier-Stokes. The figure shows the $1d$ unstable manifold of the ‘lower-branch’ steady state \mathbf{u}_{LB} (thick lines) and $2d$ portions of the unstable manifolds of the ‘new’ and ‘upper-branch’ steady states \mathbf{u}_{NB} and \mathbf{u}_{UB} . The plane of the projection is defined in terms of the *steady-state solutions*; it is *dynamically invariant* and independent of the numerical representation. See §6 for discussion.

reader is advised to go directly to §6, and backtrack to the technical preliminaries when needed. The challenges outstanding are discussed in §7.

2. Unstable coherent states: Observations and theory

In the past two decades, physicists and engineers have assembled a body of observational evidence that hydrodynamic flows exhibit organized and, in the dynamical systems sense, low-dimensional behavior for a variety of flow conditions. Experimental observations of pipe flows near the onset of turbulence (Hof *et al.* (2003, 2004)), coupled with new observational tools such as stereoscopic particle image velocimetry (van Doorne (2004)) give us a very detailed dynamical picture of wall-bounded moderate- Re turbulent shear flows. One observes ‘recurrent coherent states’ that evolve and interact in coarsely predictable ways over long time scales. The dominant structures in wall-bounded shear flows are counter-rotating ‘rolls’, and low and high-speed ‘streaks’ near flat walls.

Observed structures resemble the numerically computed unstable traveling wave solutions of Faisst & Eckhardt (2003) and Wedin & Kerswell (2004), and provide experimental evidence for the relevance of Waleffe (1998) exact coherent states. The first such unstable $3D$ steady state solution of the Navier-Stokes equations was discovered by Nagata (1990) for plane Couette flow. Figure 3 exhibits irregular but repeated roll-streak oscillations first observed by Kim *et al.* (1987), computed here for plane Couette flow with $Re = 400$. Streaky structure is evident in the plot of skin friction on the bottom wall, figure 3(d). Counter-rotating vortices are apparent in the stream-normal cross-section plot of vorticity, figure 3(b).

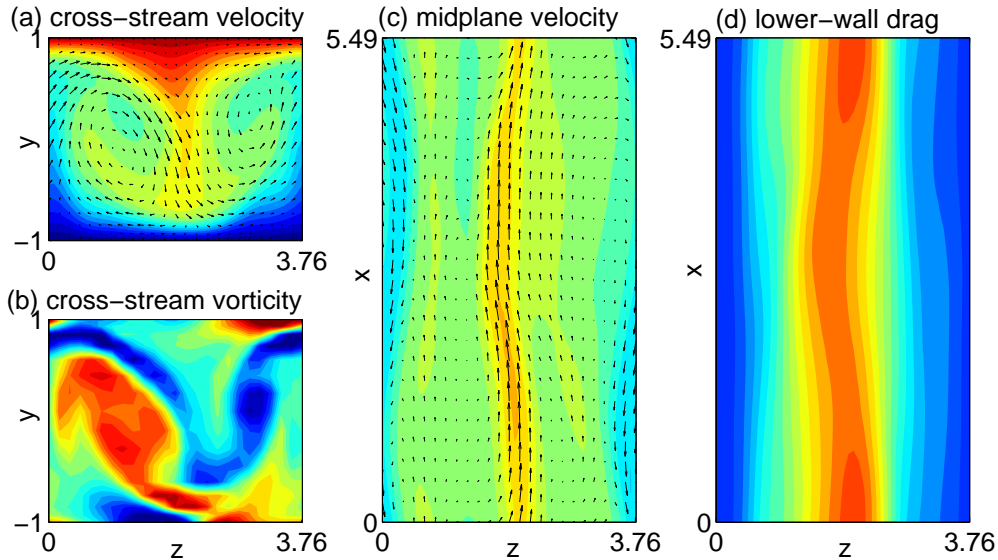


FIGURE 3. A snapshot of sustained plane Couette turbulence at $Re = 400$, Hamilton *et al.* (1995) $[L_x, L_y, L_z] = [7\pi/4, 2, 6\pi/5]$ cell, computed with `Channelflow.org` code. (a) The cross-stream velocity in the $(0, y, z)$ plane, with color indicating (red/blue or light/dark for positive/negative) streamwise (x -direction) flow u , and arrows indicating in-plane flow v, w . (b) The cross-stream vorticity in the same $(0, y, z)$ plane. (c) The velocity in the $(x, 0, z)$ plane midway between the walls at $y = \pm 1$; arrows indicate in-plane velocity u, w , the color map the streamwise flow u . (d) The drag $\partial u / \partial y$ on the $y = -1$ wall. The color map ranges from near 0 (blue) to 5 times the laminar drag (red). The rolls visible in (a) draw high-speed fluid (red) down from the upper wall, causing a high-speed streak and a high-drag streak in (d), centered at $z = L_z/2$.

These recurrent coherent states are important because of their generic occurrence in wall-bounded shear flows, and their role in transferring energy from the walls to turbulent regions. The continued circulation of high and low-speed fluid causes the high and low-speed streaks near the wall, resulting in dramatically higher drag than occurs for laminar flows. For example, the power input needed to maintain constant plane Couette flow wall velocity jumps by a factor of three if the flow goes turbulent, see figure 4 (c). The ubiquity of these structures makes them of crucial importance for understanding turbulence and its control.

Rolls and streaks appear in a simple form in plane Couette flows, where the fluid is sheared by the motion of two parallel planes moving in opposite directions at a constant speed. For moderate- Re numbers, the rolls span the full distance between the walls, as opposed to channel and boundary-layer flows, where near-wall structures are influenced by turbulence from distant regions. Even the linear stability of ‘trivial’ laminar solutions of shear flows poses serious challenges. It is rigorously established that the laminar flow is stable for all Re for plane Couette flow (Romanov (1973); Drazin & Reid (1981)), with first bifurcation pushed to ∞ (Nagata (1990)). Convenient flows to study numerically, plane Couette flows are also subject to intense experimental scrutiny (Bottin *et al.* (1998); Dauchot & Daviaud (1995); Dauchot *et al.* (1998); Tillmark & Alfredsson (1992); Tillmark (1995); Bech *et al.* (1995); Lundbladh & Johansson (1991); Hegseth *et al.* (1992); Daviaud *et al.* (1992); Malerud *et al.* (1995)).

The preponderance of recognizable recurrent coherent states in these flows suggests

that their long-time dynamics is sufficiently low-dimensional to make exploration of the geometry of their state-space attractors practically feasible. The moderate- Re turbulent regimes of shear flows are expected to have attractors of low intrinsic dimension.

Motivated by these observations, a number of researchers have attempted to derive low-dimensional dynamical-system models for boundary-layer and plane Couette flows. The Aubry *et al.* (1988); Holmes *et al.* (1996) Cornell group used ‘Proper Orthogonal Decomposition’ [POD] of experimental data and Galerkin projection of the Navier-Stokes equations to produce low-order models of structures in boundary-layer turbulence. Their models reproduce many qualitative features of the boundary layer, but the quantitative accuracy and the validity of simplifying assumptions in their derivation are uncertain (Zhou & Sirovich (1992); Sirovich & Zhou (1994); Gibson (2002)).

The first low-dimensional models of plane Couette flow were low-order models of roll-streak behavior, based on the Self-Sustaining Process theory of (Waleffe (1995, 1997)). These spurred many other studies (Dauchot & Vioujard (2000); Moehlis *et al.* (2004b); Manneville (2004)), including a 9-variable model (Skufca (2005)) and low-dimensional POD/Galerkin models (Moehlis *et al.* (2004a,c)). As the Cornell POD models, these models exhibit interesting dynamics reminiscent of plane Couette flows, and highlight the importance of preserving flow symmetries. The work of Skufca *et al.* (2006) offers an elegant dynamical systems picture, with the stable manifold of a periodic orbit defining the basin boundary that separates the turbulent and laminar attractors at low- Re ($Re < 402$), and the stable set of a higher dimensional chaotic object defining the boundary at higher Re . Based on a Schmiegel (1999) 9-variable model, this work has no predictive power for plane Couette flow, for which a fully-resolved DNS needs to be undertaken. What all existing models have in common is sensitively model-dependent dynamics and no quantitative relation to true Navier-Stokes flows. A systematic study of the convergence of POD/Galerkin models of plane Couette flow to the fully-resolved simulations indicates that at least 10^3 dimensions are needed for quantitatively predictive modeling of the plane Couette flow (Gibson (2002)).

The failure of attempts at low-dimensional modeling motivates the search for exact coherent states in fully-resolved Navier-Stokes simulations. Using a continuation technique combined with a 30×10^3 -dimensional Newton search, Waleffe (1998, 2001, 2003) succeeded in numerically calculating families of exact 3D steady states and traveling waves of Navier-Stokes in plane Couette and Poiseuille flows, for a variety of boundary conditions and Re numbers. These ‘exact coherent states’ turn out to be remarkably similar to turbulent structures observed in DNS and experiment. Waleffe’s ‘upper-branch’ solution captures many statistical features of turbulent plane Couette flow and the roll-streak structures shown in figure 3. In computations, spanwise-streamwise periodic cells are chosen to be sufficiently large for the empirically observed sustained turbulence. Whether such small periodic cells actually sustain turbulence for a given choice of cell size is a subtle dynamical issue: Schmiegel & Eckhardt (1997); Schmiegel (1999) observe only chaotic transients in their study of small-cell plane Couette flow.

Traveling waves have been found for pipe flow (Faisst & Eckhardt (2003); Wedin & Kerswell (2004)) and observed in beautiful experiments using stereoscopic particle image velocimetry (Hof *et al.* (2004); Busse (2004); Barenghi (2004)). Preliminary evidence of the relevance of steady solutions to sustained turbulence and transition to turbulence is discussed by Waleffe (2003) and Jiménez *et al.* (2005). The next important advance was the determination of the first short-period unstable periodic solution of full 3D Navier-Stokes by Kawahara & Kida (2001), a solution that appears well embedded into plane Couette flow’s natural ergodic measure, capturing the basic statistics of plane Couette flow more closely than Waleffe’s nearby upper-branch solution (see figure 4). Further periodic or-

bits and relative periodic orbits were computed by Viswanath (2007b). Other important recent advances are detailed studies of the lower-branch solution and its neighborhood which is conjectured (Waleffe & Wang (2005); Wang *et al.* (2007); Viswanath (2007a)) to control the basin boundary between the turbulent and laminar attractors.

3. Plane Couette flow

Plane Couette flow is comprised of an incompressible viscous fluid confined between two infinite parallel plates moving in opposite directions at constant and equal velocities. The flow obeys no-slip boundary conditions at the walls. The Reynolds number is defined as $Re = UL/\nu$, where ν is the kinematic viscosity of the fluid, U is the plate velocity, and L is the length scale, taken to be half the distance between the plates. After rescaling U , L , and fluid density to unity, the Navier-Stokes equations are

$$\frac{\partial \mathbf{u}}{\partial t} + \mathbf{u} \cdot \nabla \mathbf{u} = -\nabla p + \frac{1}{Re} \nabla^2 \mathbf{u}, \quad \nabla \cdot \mathbf{u} = 0.$$

The direction of the plate motion is along the “streamwise” x -axis, the direction normal to the plates is the “wall-normal” y -axis, $y \in [-1, +1]$, and the in-plane z -axis, normal to the plate velocity, is referred to as “spanwise.” The x, y, z unit vectors are $\hat{\mathbf{x}}, \hat{\mathbf{y}}, \hat{\mathbf{z}}$ (we use boldface exclusively to indicate vectors in three spatial dimensions). The velocity field \mathbf{u} has streamwise, wall-normal, and spanwise components $\mathbf{u} = [u, v, w]$; the velocity at a point \mathbf{x} and time t is $\mathbf{u}(\mathbf{x}, t) = [u, v, w](x, y, z, t)$. The velocity obeys no-slip boundary conditions at the walls, $\mathbf{u}(x, \pm 1, z) = [0, \pm 1, 0]$. We assume that the spatial mean of the pressure gradient is zero, *i.e.*, that there is no pressure drop across the length of the cell.

In simulations, the infinite x and z directions are replaced with a periodic cell of lengths L_x and L_z . We denote the periodic domain of the cell by $\Omega = [0, L_x] \times [-1, 1] \times [0, L_z]$. Cell sizes are also sometimes defined in terms of cell wavenumbers $\alpha = 2\pi/L_x$ and $\gamma = 2\pi/L_z$. A few of our computations are performed in the Hamilton *et al.* (1995) $[L_x, L_y, L_z] = [7\pi/4, 2, 6\pi/5]$ cell which exhibits empirical sustained turbulence, but, unless noted otherwise, all results discussed here are for the plane Couette flow at $Re = 400$, $[L_x, L_y, L_z] = [2\pi/1.14, 2, 4\pi/5]$ cell used by Waleffe (2003) in calculation of exact 3D upper-branch and lower-branch steady states. Though this cell is too small to sustain turbulence, it serves well to illustrate our invariant manifolds construction in context of transient dynamics on the way to the laminar state.

Replacing \mathbf{u} with $\mathbf{u} + y \hat{\mathbf{x}}$ recasts Navier-Stokes in terms of the deviation of the velocity from laminar flow:

$$\frac{\partial \mathbf{u}}{\partial t} + y \frac{\partial \mathbf{u}}{\partial x} + v \hat{\mathbf{x}} + \mathbf{u} \cdot \nabla \mathbf{u} = -\nabla p + \frac{1}{Re} \nabla^2 \mathbf{u}, \quad \nabla \cdot \mathbf{u} = 0. \quad (3.1)$$

The deviation \mathbf{u} satisfies no-slip boundary conditions at the walls, $\mathbf{u}(x, \pm 1, z) = 0$. Henceforth we refer to the deviation \mathbf{u} as “velocity” and $\mathbf{u} + y \hat{\mathbf{x}}$ as “total velocity,” and we take (3.1) as the Navier-Stokes equations for plane Couette flow.

3.1. Energy transfer rates

The kinetic energy density of total velocity field is given by:

$$E(t) = \frac{1}{V} \int_{\Omega} d\mathbf{x} \frac{1}{2} |\mathbf{u} + y \hat{\mathbf{x}}|^2 = \frac{1}{6} + \frac{1}{V} \int_{\Omega} d\mathbf{x} \left(u y + \frac{1}{2} |\mathbf{u}|^2 \right) \quad (3.2)$$

where $V = 2L_x L_z$. In plane Couette flow, energy is injected through the motion of the walls and dissipated by fluid viscosity,

$$\dot{E} = I - D, \quad (3.3)$$

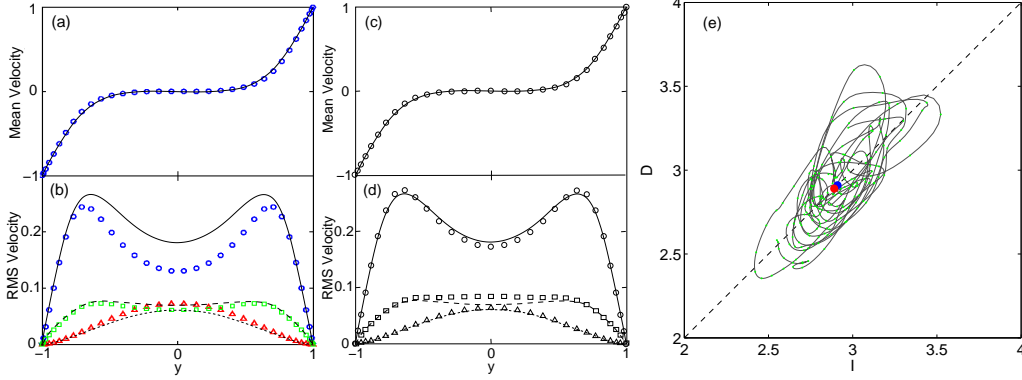


FIGURE 4. (a), (b) Mean and RMS velocity profiles, Waleffe (2003) \mathbf{u}_{UB} steady state (symbols), $[L_x, L_y, L_z] = [2\pi/1.14, 2, 4\pi/5]$ cell. (c), (d) Mean and RMS velocity profiles for the Kawahara & Kida (2001) periodic solution (symbols), Hamilton *et al.* (1995) $[L_x, L_y, L_z] = [7\pi/4, 2, 6\pi/5]$ cell. (a), (c) Circles: $\overline{u(y)}$. (b), (d) Circles: $\overline{u_{rms}}$, squares: v_{rms} , triangles: w_{rms} . (e) $(I(t), D(t))$ fluctuation over a typical sustained turbulence trajectory segment (blue line), ran for time $t = 1000$, Hamilton *et al.* (1995) cell. The laminar steady state dissipation rate $D = I = 1$ is at (1, 1), the mean dissipation rate over Kawahara & Kida (2001) periodic orbit $\overline{D} = \overline{I} = 2.91$ is marked by a blue dot, and the typical turbulent trajectory mean dissipation rate $\overline{D} = 2.89$ by the red dot. (c), (d) continuous lines: typical turbulent trajectory mean and RMS velocity profiles. The same continuous lines are overlaid over (a), (b) Waleffe (2003) cell (which exhibits transient turbulence only) to guide the eye.

where I is the power input and D is the bulk viscous dissipation rate. We normalize E , D , and I so that laminar flow has $D = I = 1$. The dissipation rate is given by

$$D(t) = \frac{1}{V} \int_{\Omega} d\mathbf{x} |\nabla \times (\mathbf{u} + y \hat{\mathbf{x}})|^2 = 1 + \frac{1}{V} \int_{\Omega} d\mathbf{x} \left(2 \frac{\partial u}{\partial y} - 2 \frac{\partial v}{\partial x} + |\nabla \times \mathbf{u}|^2 \right). \quad (3.4)$$

For a visualization of the integrand see the instantaneous vorticity field depicted in figure 3 (b).

The power input I is the instantaneous drag at the wall, or the the power needed to maintain constant wall velocity $U = \pm 1$:

$$I(t) = 1 + \frac{1}{2A} \int_A dx dz \left(\frac{\partial u}{\partial y} \Big|_{y=1} + \frac{\partial u}{\partial y} \Big|_{y=-1} \right), \quad A = L_x L_z. \quad (3.5)$$

For a visualization of the integrand see the plot of instantaneous skin friction for turbulent plane Couette flow, figure 3 (d).

Plots of I vs. D , such as figure 4 (e), provide insights into energetics of a turbulent flow, and into the dynamical structure of its state-space. Steady states and traveling waves must fall on the line $I = D$ where these two quantities are in balance. The energy input and dissipation rates also balance each other over in averages over a single period of a periodic orbit or relative periodic orbit p ,

$$D_p = \frac{1}{T_p} \int_0^{T_p} dt D(t) = \frac{1}{T_p} \int_0^{T_p} dt I(t) = I_p, \quad (3.6)$$

as well as for long-time averages, $\overline{I(t)} = \overline{D(t)}$.

We note that the turbulent trajectory in figure 4 stays clear of the much lower \mathbf{u}_{LB} and \mathbf{u}_{NB} dissipation rates $(D_{LB}, D_{NB}) = (1.429, 1.454)$, so these invariant solutions are far from the turbulent attractor. However, projections from the ∞ -dimensional state-space onto the 3d (E, I, D) representation of the flow can be misleading. For example,

the energy, the dissipation rate and the mean and RMS velocity profiles of both Waleffe (2003) \mathbf{u}_{UB} steady state and Kawahara & Kida (2001) periodic orbit are all numerically close to the long-time turbulent averages, but states that are clearly separated in the full state-space can overlay each other in such low-dimensional projections. Optimistic hopes that “turbulence” is different from low-dimensional chaos, insofar that the determination of one magic periodic orbit could yield all long-time predictions, are misplaced. As always, here too one needs a hierarchy of periodic orbits of increasing length to obtain accurate predictions (Cvitanović *et al.* (2006)).

3.2. Symmetries of plane Couette flow

The Navier-Stokes equations for plane Couette flow are invariant under two reflections, $\partial(\sigma_j \mathbf{u})/\partial t = \sigma_j(\partial \mathbf{u}/\partial t)$, and a continuous two-parameter group of translations, $\partial(\tau \mathbf{u})/\partial t = \tau(\partial \mathbf{u}/\partial t)$,

$$\begin{aligned} \sigma_1 [u, v, w](x, y, z) &= [u, v, -w](x, y, -z) \\ \sigma_2 [u, v, w](x, y, z) &= [-u, -v, w](-x, -y, z) \\ \tau(\ell_x, \ell_z)[u, v, w](x, y, z) &= [u, v, w](x + \ell_x, y, z + \ell_z). \end{aligned} \quad (3.7)$$

The plane Couette symmetries call for a geometrical interpretation in the space of fluid velocity fields. Let \mathbb{U} be the space of square-integrable, real-valued velocity fields that satisfy the kinematic conditions of plane Couette flow:

$$\begin{aligned} \mathbb{U} &= \{ \mathbf{u} \in L^2(\Omega) \mid \nabla \cdot \mathbf{u} = 0, \mathbf{u}(x, \pm 1, z) = 0, \\ &\quad \mathbf{u}(x, y, z) = \mathbf{u}(x + L_x, y, z) = \mathbf{u}(x, y, z + L_z) \}. \end{aligned} \quad (3.8)$$

The continuous symmetry $\tau(\ell_x, \ell_z)$ maps each point $\mathbf{u} \in \mathbb{U}$ to a $2d$ torus of points with identical dynamic behavior, so in general any single point in phase space belongs to a $2d$ family of dynamically equivalent states of the fluid. \mathbb{U} is also invariant under any subgroup of the translation group. Of particular interest for this investigation is the discrete Abelian D_2 dihedral 4-element group of half-cell translations

$$T = \{1, \tau_x, \tau_z, \tau_{xz}\}, \quad \tau_x = \tau(L_x/2, 0), \quad \tau_z = \tau(0, L_z/2), \quad \tau_{xz} = \tau_x \tau_z. \quad (3.9)$$

In our discussion of equilibria, the simplest invariant solutions of plane Couette flow, we shall focus our attention on \mathbb{U}_S , a symmetric subspace of \mathbb{U} defined by two symmetries satisfied by the Waleffe (2003) equilibria: the ‘shift-reflect’ symmetry $s_1 = \tau_x \sigma_1$; and ‘shift-rotate’ symmetry $s_2 = \tau_{xz} \sigma_2$. These symmetries generate the discrete group $S = \{1, s_1, s_2, s_3\}$, where $s_3 = s_1 s_2$, which is isomorphic to the dihedral group D_2 . The group acts on velocity fields \mathbf{u} as

$$\begin{aligned} s_1 [u, v, w](x, y, z) &= [u, v, -w](x + L_x/2, y, -z) \\ s_2 [u, v, w](x, y, z) &= [-u, -v, w](-x + L_x/2, -y, z + L_z/2) \\ s_3 [u, v, w](x, y, z) &= [-u, -v, -w](-x, -y, -z + L_z/2). \end{aligned} \quad (3.10)$$

Symmetries of a fluid state \mathbf{u} are determined by computing their projections

$$P_j^\pm \mathbf{u} = \frac{1}{2}(1 \pm s_j) \mathbf{u}. \quad (3.11)$$

A state \mathbf{u} is symmetric with respect to a given s_j if $\|P_j^- \mathbf{u}\| = 0$, antisymmetric if $\|P_j^+ \mathbf{u}\| = 0$, and otherwise belongs to a multiplet of fluid states mapped into each other by s_j . This symmetry test usually requires determination of a $2d$ shift τ that aligns the (x, z) origin with the s_j definition (3.10).

Denote by

$$\mathbb{U}_S = \{\mathbf{u} \in \mathbb{U} \mid \mathbf{u} = s_j \mathbf{u}, s_j \in S\} \quad (3.12)$$

the fully symmetric subspace of plane Couette flow velocity fields invariant under S . Projection of an arbitrary state \mathbf{u} into \mathbb{U}_S is the product of two symmetrizations (3.11):

$$P_1^+ P_2^+ \mathbf{u} = \frac{1}{4}(1 + s_1 + s_2 + s_3) \mathbf{u}.$$

The two reflection symmetry planes intersect the torus of continuous translations in four points, so \mathbb{U}_S is also invariant under the discrete group of half-cell translations (3.9). Then, for each velocity field $\mathbf{u} \in \mathbb{U}_S$ the three half-cell translations $\tau_x \mathbf{u}$, $\tau_z \mathbf{u}$, and $\tau_{xz} \mathbf{u}$ are also in \mathbb{U}_S . In general these will be four distinct states, so the restriction to the \mathbb{U}_S subspace reduces the 2-torus of equivalent solutions related by translation to four distinct, but equivalent, states.

4. Plane Couette flow as a dynamical system

The Navier-Stokes equations consist of a partial differential evolution equation and constraint equations for the boundary and incompressibility conditions. To represent plane Couette as a dynamical system and to compute its invariant solutions, we must construct a finite-dimensional representation of fluid state, eliminate the constraint equations, and replace the infinite-dimensional PDE with a finite-dimensional representation of dynamics. Our approach to the first two problems is to represent velocity fields in terms of a basis that incorporates the boundary and incompressibility constraints. In §4.1 we construct a finite-dimensional dynamical-systems representation of plane Couette flow with states $a \in \mathbb{R}^d$ and dynamics $\dot{a} = F(a)$ in terms of such a basis. An explicit construction of the basis is given in §4.2.

In the very high dimensions necessary for accurate representation of the flow, the ODE system is too large for practical use. In §4.3 and §5 we address how CFD algorithms can be employed to efficiently calculate state-space dynamics, invariant solutions, and their linear stability.

Much of this work is based on the algorithms of Viswanath (2007b) and the 3D unstable equilibrium ‘exact coherent states’ first computed by Waleffe (2003). Our perspective, however, is somewhat different: we visualize the discretized representation of a fluid state as a finite-dimensional *state-space* vector, and the action of Navier-Stokes equations as a *dynamical system trajectory* in this state-space. We are motivated in equal parts by Hopf’s vision, and by the POD work of Aubry *et al.* (1988), Holmes *et al.* (1996), and Smith *et al.* (2005), which injected dynamical systems notions such as state-space geometry and continuous symmetries into low-dimensional models of boundary shear flows. Here we port these dynamical insights to more recent high-dimensional approaches to computing exact invariant solutions.

4.1. ODE representation of plane Couette flow

Consider the expansion of velocity fields $\mathbf{u} \in \mathbb{U}$,

$$\mathbf{u}(\mathbf{x}, t) = \sum_{n=1}^d a_n(t) \Phi_n(\mathbf{x}), \quad (4.1)$$

in a basis set $\Phi_n \in \mathbb{U}$, i.e. real-valued functions $\Phi_n(\mathbf{x})$ that individually satisfy periodicity in x and z , no-slip boundary conditions at the walls, and incompressibility:

$$\begin{aligned}\Phi_n(x + L_x, y, z) &= \Phi_n(x, y, z), & \Phi_n(x, \pm 1, z) &= 0, \\ \Phi_n(x, y, z + L_z) &= \Phi_n(x, y, z), & \nabla \cdot \Phi_n &= 0.\end{aligned}\quad (4.2)$$

Let the basis be orthonormal, $(\Phi_m, \Phi_n) = \delta_{mn}$, with respect to the inner product and norm

$$(\mathbf{u}, \mathbf{v}) = \frac{1}{V} \int_{\Omega} d\mathbf{x} \mathbf{u} \cdot \mathbf{v}, \quad \|\mathbf{u}\|^2 = (\mathbf{u}, \mathbf{u}), \quad (4.3)$$

so that

$$a_n = (\mathbf{u}, \Phi_n). \quad (4.4)$$

Substitute (4.1) into Navier-Stokes equation (3.1), and take the inner product of both sides against Φ_m . The pressure term vanishes due to the no-slip and incompressibility conditions and vanishing spatial-mean pressure gradient, assumed in §3 as an external condition of the flow. This results in an ODE of the form

$$\dot{a}_m = F_m(a) = \sum_{n=1}^d L_{mn} a_n + \sum_{n=1}^d \sum_{n'=1}^d N_{mnn'} a_n a_{n'}, \quad (4.5)$$

where $a = (a_1, \dots, a_d) \in \mathbb{R}^d$ is the state-space vector (4.4) representing the state of the instantaneous velocity field $\mathbf{u}(\mathbf{x}, t)$ over the whole cell domain Ω . The linear operator is given by

$$L_{mn} = - \left(y \frac{\partial \Phi_n}{\partial x} + \Phi_n^v \hat{x}, \Phi_m \right) + \frac{1}{Re} (\nabla^2 \Phi_n, \Phi_m), \quad (4.6)$$

where Φ_n^v is the \hat{y} component of Φ_n . The nonlinear advection operator term is

$$N_{mnn'} = - (\Phi_n \cdot \nabla \Phi_{n'}, \Phi_m). \quad (4.7)$$

This derivation can be put on sounder footing by expanding (3.1) in the finite basis and minimizing the projection of the residual on the same basis.

The linearized dynamics at state a are governed by the stability matrix

$$DF_{mn}|_a = \left. \frac{\partial F_m}{\partial a_n} \right|_a = L_{mn} + \sum_{n'=1}^d (N_{mnn'} + N_{mn'n}) a_{n'}. \quad (4.8)$$

The state-space trajectory $a(t)$ induced by the Navier-Stokes flow is given by the integral

$$a(t) = f^t(a) = a + \int_0^t d\tau F(a). \quad (4.9)$$

4.2. Construction of divergence-free basis

In this section we explicitly construct a basis set that meets the conditions set out in the previous section (4.2). The boundary conditions of \mathbb{U} suggest a basis for velocity fields comprised of Fourier modes in x and z and polynomials in y . In anticipation of §4.3, we construct finite basis sets with exactly one element per degree of freedom in the Fourier \times Chebyshev \times Chebyshev CFD algorithm for plane Couette flow.

Our construction follows the Moser *et al.* (1983) discretization of the Navier-Stokes equation (see also Canuto *et al.* (1988)) with a few modifications that aid its use as a state-space representation: (1) the basis elements are real-valued, (2) Legendre polynomials and a uniform weighting function are used instead of Chebyshev polynomials

and non-uniform weighting, and (3) the basis set is orthogonal and normalized. These choices are a matter of convenience. For example, real-valued basis functions produce independent real-valued coefficients a_n and real-valued elements in L_{mn} and $N_{mnn'}$. Complex-valued functions lead to more compact expressions, but they produce almost twice as many variables related by complex symmetry constraints.

Let \mathbb{U}^{JKL} be the subspace of \mathbb{U} spanned by Fourier modes of maximum order J, K and polynomials of maximum order L . We seek to construct a complete and linearly independent basis for \mathbb{U}^{JKL} with Fourier modes in x, z and polynomials in y that satisfy the boundary and incompressibility conditions of \mathbb{U} . Real-valued Fourier modes may be represented by

$$g_j(x) = \begin{cases} \sin jx & j < 0 \\ 1 & j = 0 \\ \cos jx & j > 0 \end{cases}. \quad (4.10)$$

Derivatives of g_j satisfy $g'_j(x) = jg_{-j}(x)$. Consider basis functions $\Phi(\mathbf{x})$ of form

$$\begin{aligned} \Phi_{\sigma jkl}(\mathbf{x}) = & \Phi_{\sigma jkl}^u(y)g_j(\alpha x)g_{-k}(\gamma z)\hat{\mathbf{x}} + \\ & \Phi_{\sigma jkl}^v(y)g_{-j}(\alpha x)g_{-k}(\gamma z)\hat{\mathbf{y}} + \\ & \Phi_{\sigma jkl}^w(y)g_{-j}(\alpha x)g_k(\gamma z)\hat{\mathbf{z}}, \end{aligned} \quad (4.11)$$

where α and γ are the cell-size wavenumbers given by $\alpha = 2\pi/L_x$ and $\gamma = 2\pi/L_z$.

A complete and linearly independent basis for \mathbb{U}^{JKL} can be constructed by letting the Fourier indices range over $-J \leq j \leq J$, $-K \leq k \leq K$, and choosing (Φ^u, Φ^v, Φ^w) as linearly independent polynomial triplets in y up to order L that satisfy the no-slip boundary conditions at $y = \pm 1$ and the divergence condition

$$\alpha j \Phi_{\sigma jkl}^u(y) + \frac{\partial}{\partial y} \Phi_{\sigma jkl}^v(y) + \gamma k \Phi_{\sigma jkl}^w(y) = 0. \quad (4.12)$$

Two of the three functions $\Phi_{\sigma kjl}^u, \Phi_{\sigma kjl}^v, \Phi_{\sigma kjl}^w$ can be set independently and the third derived from incompressibility. These two possibilities are distinguished with the index $\sigma \in \{0, 1\}$. Canuto *et al.* (2006) prescribe the no-slip conditions by defining the polynomial triplets as differences of Legendre polynomials $P_l(y)$:

$$R_l(y) = P_{l-2}(y) - P_l(y) \quad \text{for } l \geq 2, \quad (4.13)$$

$$Q_l(y) = \frac{1}{2l+1}R_{l+1}(y) - \frac{1}{2l-3}R_{l-1}(y) \quad \text{for } l \geq 3. \quad (4.14)$$

Note that $R_l(\pm 1) = 0$ for $l \geq 2$, that $Q_l(\pm 1) = Q'_l(\pm 1) = 0$ for $l \geq 3$, and that the polynomial order of Q_l is $l + 1$.

Table 1 enumerates the set of linearly independent polynomial triplets satisfying the above conditions for each combination of j and k . These elements can be combined as in (4.11) to construct a complete basis for a given \mathbb{U}^{JKL} . Basis elements $\Phi_{\sigma jkl}$ in table 1 are linearly independent but not orthogonal. In our computations we represent the polynomials in y numerically and orthonormalize $\Phi_{\sigma jkl}$ by a modified Gram-Schmidt orthogonalization algorithm as described in Trefethen & Bau (1997). The orthogonalization is block triangular; it leaves the Fourier and polynomial degree of a given element unchanged.

The dimension d of \mathbb{U}^{JKL} and \mathbb{R}^d is given by the number of independent triplets in table 1:

$$d = 4(J + 2JK + K)(L - 2) + 2(L - 1) \quad (4.15)$$

σ	j	k	l	$\Phi_{\sigma jkl}^u(y)$	$\Phi_{\sigma jkl}^v(y)$	$\Phi_{\sigma jkl}^w(y)$	# modes
0	0	0	$\{2, \dots, L\}$	$R_l(y)$	0	0	$L-1$
1	0	0	$\{2, \dots, L\}$	0	0	$R_l(y)$	$L-1$
0	j	0	$\{2, \dots, L\}$	0	0	$R_l(y)$	$2J(L-1)$
1	j	0	$\{3, \dots, L-1\}$	$R_l(y)$	$-\alpha j Q_l(y)$	0	$2J(L-3)$
0	0	k	$\{2, \dots, L\}$	$R_l(y)$	0	0	$2K(L-1)$
1	0	k	$\{3, \dots, L-1\}$	0	$-\gamma k Q_l(y)$	$R_l(y)$	$2K(L-3)$
0	j	k	$\{2, \dots, L\}$	$\gamma k R_l(y)$	0	$-\alpha j R_l(y)$	$4JK(L-1)$
1	j	k	$\{3, \dots, L-1\}$	$\gamma k R_l(y)$	$-\alpha \gamma j k Q_l(y)$	$\alpha j R_l(y)$	$4JK(L-3)$

TABLE 1. The polynomial triplets for a complete set of linearly independent basis functions $\Phi_{\sigma jkl}$ for \mathbb{U}^{JKL} , the space of allowed velocity deviations up to Fourier order J, K and polynomial degree L . Indices j and k are non-zero, $1 \leq |j| \leq J$ and $1 \leq |k| \leq K$, unless explicitly marked as zero.

In what follows d refers to the dimension of state-space representation, while $D = 3$ refers to the spatial dimension of Navier-Stokes equation.

4.3. Relation between state-space and CFD representations

As noted earlier, the ODE representation of dynamics is too large for numerical computation. The number of non-zero elements in the linear operator L_{mn} is $O(4JKL^2) \approx 10^6$, and the nonlinear operator N_{mnp} has $O(16J^2K^2L^3) \approx 10^{10}$ non-zero elements for the discretizations used in this study. To store such an object would require terabytes of computer memory, well beyond what is practically sensible. It is much more sensible to calculate dynamics with a CFD algorithm.

However, other computations are more conveniently performed in the absence of constraints, with fluid states represented as points $a \in \mathbb{R}^d$. In practice, we use the representation best suited to a particular purpose. Vectors $a \in \mathbb{R}^d$ form our primary representation of fluid state, for example, as the unknown variables in a Newton search for an equilibrium solution of plane Couette flow. The evolution of state $a(t)$ in time is determined by converting to the CFD algorithm representation of \mathbf{u} , integrating the CFD algorithm, and projecting back to $a(t+T)$:

$$\begin{array}{ccc}
 \mathbb{R}^d & & \text{CFD} \\
 a(t) & \xrightarrow{\mathbf{u} = \sum a_n \Phi_n} & \mathbf{u}(\mathbf{x}, t) \\
 & & \downarrow f_{\text{CFD}}^T \\
 a(t+T) & \xleftarrow{a_n = (\mathbf{u}, \Phi_n)} & \mathbf{u}(\mathbf{x}, t+T)
 \end{array} \tag{4.16}$$

Our CFD algorithm is based on the velocity-pressure algorithm of Kleiser & Schuman (1980). The velocity field is expanded as

$$\mathbf{u}(\mathbf{x}, t) = \sum_{j=-J}^J \sum_{k=-K}^K \sum_{\ell=0}^L \sum_{m=1}^3 \hat{u}_{jklm} T_\ell(y) e^{2\pi i(jx/L_x + kz/L_z)} \hat{\mathbf{x}}_m, \tag{4.17}$$

where the T_ℓ are Chebyshev polynomials and $(\hat{\mathbf{x}}_1, \hat{\mathbf{x}}_2, \hat{\mathbf{x}}_3) = (\hat{\mathbf{x}}, \hat{\mathbf{y}}, \hat{\mathbf{z}})$ unit vectors, and where boundary and incompressibility constraints are enforced numerically. Given these constraints, the function spaces spanned by (4.17) and the basis set enumerated in table 1 are identical, namely, \mathbb{U}^{JKL} . Further, since the basis elements are orthonormal with

respect to the inner product (4.3), inner products and norms in \mathbb{R}^d are equal to the inner products and norms of corresponding velocity fields in \mathbb{U}^{JKL} . That is, if a and b are the state-space vectors for the fields \mathbf{u} and \mathbf{v} , then $a \cdot b = (\mathbf{u}, \mathbf{v})$ and $|a|^2 = \|\mathbf{u}\|^2$. Thus the state-space representation is an orthonormal parameterization of the space of velocity fields, and its norm is related to the physical energy of the fluid velocity field.

For further discussion of the CFD algorithm and conversion between state-space and CFD representations, see § A.1.

5. Invariant solutions and linear stability

Let $\mathbf{F}_{\text{NS}}(\mathbf{u})$ represent the Navier-Stokes equation (3.1) and \mathbf{f}_{NS}^t its time- t forward map for the given geometry, boundary conditions, and Reynolds number:

$$\frac{\partial \mathbf{u}}{\partial t} = \mathbf{F}_{\text{NS}}(\mathbf{u}), \quad \mathbf{f}_{\text{NS}}^t(\mathbf{u}) = \mathbf{u} + \int_0^t d\tau \mathbf{F}_{\text{NS}}(\mathbf{u}). \quad (5.1)$$

We seek invariant solutions (exact coherent states) of Navier-Stokes of the following types:

$$\begin{aligned} \mathbf{F}_{\text{NS}}(\mathbf{u}_{\text{EQ}}) &= 0 && \text{steady-state or equilibrium } \mathbf{u}_{\text{EQ}} \\ \mathbf{F}_{\text{NS}}(\mathbf{u}_{\text{EQ}}) &= -\mathbf{c} \cdot \nabla \mathbf{u}_{\text{EQ}} && \text{traveling wave or relative equilibrium } \mathbf{u}_{\text{EQ}}, \text{ velocity } \mathbf{c} \\ \mathbf{f}_{\text{NS}}^{T_p}(\mathbf{u}_p) &= \mathbf{u}_p && \text{periodic orbit } p \text{ of period } T_p \\ \mathbf{f}_{\text{NS}}^{T_p}(\mathbf{u}_p) &= \tau_p \mathbf{u}_p && \text{relative periodic orbit, period } T_p, \text{ shift } \tau_p = \tau(\ell_x, \ell_z). \end{aligned} \quad (5.2)$$

Continuous symmetries of plane Couette flow allow for relative equilibria and relative periodic orbits, as well as equilibria and periodic orbits. We expect to see many more relative periodic orbits than periodic orbits because a trajectory that starts on and returns to a given torus is unlikely to intersect it at the initial point, unless forced to do so by a discrete symmetry. This indeed is the case for other PDEs with continuous symmetries, such as the complex Ginzburg-Landau equation (López *et al.* (2006)) and the Kuramoto-Sivashinsky equation (Cvitanović *et al.* (2007)). However, the equilibria studied here lie within the invariant symmetric subspace \mathbb{U}_s defined in (3.12). Restriction to \mathbb{U}_s eliminates relative equilibria and relative periodic orbits. In this paper, we focus mostly on the dynamics and equilibria within this invariant subspace.

5.1. Solutions of linearized dynamics

Computing invariant solutions and their eigenvalues was technically the most challenging part of this project. The state-space representation of the equilibrium equations provides a discrete system that can be solved numerically. For example, equilibria are computed as solutions of

$$\dot{a} = F(a) = 0, \quad (5.4)$$

and the eigenvalues λ and eigenvectors b are computed from the stability matrix DF ,

$$DF|_a b = \lambda b. \quad (5.5)$$

The state-space representations are convenient forms for numerical computation, since they eliminate all constraints and allow for Newton search and eigenvalue calculations in the unconstrained space \mathbb{R}^d .

However, as mentioned in § 4.3, direct solution of (5.4–5.5) is impractical in the 10^4 – 10^5 dimensions needed to resolve the flow. In practice, we solve these equations in terms

of the finite-time map f^T , using Krylov-subspace methods for linear algebra calculations and a CFD algorithm for evaluation of f^T (Viswanath (2007b)). The details of the Krylov algorithms are discussed in § A.2 and § A.3.

Leaving the computational issues aside, let a_{EQ} be a solution of (5.4) and λ, b_{EQ} be a real-valued solution of (5.5) at a_{EQ} .† The linearized state-space dynamics $\dot{b} = DF|_{a_{\text{EQ}}} b$ about the equilibrium a_{EQ} has the solution $b(t) = e^{\lambda t} b_{\text{EQ}}$. For the initial condition $a(0) = a_{\text{EQ}} + \epsilon b_{\text{EQ}}$ with $\epsilon |b_{\text{EQ}}| \ll 1$, the state a evolves as

$$a(t) = a_{\text{EQ}} + \epsilon b_{\text{EQ}} e^{\lambda t} + O(\epsilon^2). \quad (5.6)$$

The corresponding steady-state velocity field is given by $\mathbf{u}_{\text{EQ}} = \sum_{n=1}^d a_{\text{EQ},n} \Phi_n$, and the corresponding eigenvalue, eigenfunction pair for the linearized Navier-Stokes equation is $\lambda, \mathbf{v}_{\text{EQ}} = \sum_{n=1}^d b_{\text{EQ},n} \Phi_n$. Small perturbations about \mathbf{u}_{EQ} along the eigenfunction \mathbf{v}_{EQ} evolve as

$$\mathbf{u}(t) = \mathbf{u}_{\text{EQ}} + \epsilon \mathbf{v}_{\text{EQ}} e^{\lambda t} + O(\epsilon^2). \quad (5.7)$$

Since physical fluids and CFD algorithms are real-valued, complex eigenvalues and eigenvectors need to be recast into a real form. Let $\lambda^{(n,n+1)} = \mu \pm i\omega$ be a pair of complex eigenvalues with eigenvectors $b_{\text{EQ}}^{(n)}, b_{\text{EQ}}^{(n+1)}$. Let

$$\begin{aligned} b^+ &= \text{Re} \left(b_{\text{EQ}}^{(n)} + b_{\text{EQ}}^{(n+1)} \right), \\ b^- &= \text{Im} \left(b_{\text{EQ}}^{(n)} - b_{\text{EQ}}^{(n+1)} \right), \\ \mathbf{v}^\pm &= \sum_{n=1}^d b_n^\pm \Phi_n. \end{aligned} \quad (5.8)$$

Then the initial condition $a(0) = a_{\text{EQ}} + \epsilon b^+$ evolves as a real-valued spiral

$$a(t) = a_{\text{EQ}} + \epsilon (b^+ \cos \omega t - b^- \sin \omega t) e^{\mu t} + O(\epsilon^2) \quad (5.9)$$

and the real-valued initial velocity field $\mathbf{u}(0) = \mathbf{u}_{\text{EQ}} + \epsilon \mathbf{v}^+$ evolves as

$$\mathbf{u}(t) = \mathbf{u}_{\text{EQ}} + \epsilon (\mathbf{v}^+ \cos \omega t - \mathbf{v}^- \sin \omega t) e^{\mu t} \quad (5.10)$$

5.2. Unstable manifolds

The trajectories $\mathbf{u}(t)$ given by (5.7) and (5.10) lie within W_{EQ}^u , the global stable / unstable manifold of equilibrium \mathbf{u}_{EQ} . If \mathbf{u}_{EQ} and \mathbf{v}_{EQ} (or $\mathbf{v}_{\text{EQ}}^\pm$) lie in a symmetric subspace \mathbb{U}_s , the corresponding stable / unstable manifold trajectory $\mathbf{u}(t)$ will stay within \mathbb{U}_s . For each real-valued unstable eigenvalue $\lambda^{(n)}$, we shall refer to the orbit of an infinitesimal perturbation (5.7) of the \mathbf{u}_{EQ} equilibrium along the corresponding eigenfunction $\mathbf{v}_{\text{EQ}}^{(n)}$ of the linearized Navier-Stokes equation as $W_{\text{EQ}}^{u,(n)}$. This part of the \mathbf{u}_{EQ} unstable manifold is 1-dimensional and can be computed by DNS integration of the initial conditions $\mathbf{u}_{\text{EQ}} \pm \epsilon \mathbf{v}_{\text{EQ}}^{(n)}$, where $\epsilon \ll 1$. For unstable complex eigenvalues, $W_{\text{EQ}}^{u,(n,n+1)}$ denotes the orbit of a *continuous circle* of perturbations of infinitesimal radius in the plane about \mathbf{u}_{EQ} spanned by $\mathbf{v}_{\text{EQ}}^{\pm,(n,n+1)}$. This part of the \mathbf{u}_{EQ} unstable manifold is 2-dimensional; its shape can be approximated by computing a set of trajectories with initial conditions $\mathbf{u}_{\text{EQ}} \pm \epsilon (\mathbf{v}_{\text{EQ}}^+ \cos \theta + \mathbf{v}_{\text{EQ}}^- \sin \theta)$ for a variety of values of θ . The global unstable manifolds

† We indicate particular invariant solutions with subscripts, such as a_{LB} or \mathbf{u}_{LB} for the low-branch equilibrium solution. The m th eigenvalue is $\lambda^{(n)}$, $n = 1, 2, \dots$, in order of decreasing real part. Whenever the context allows it, we shall omit the eigenvalue and/or solution labels.

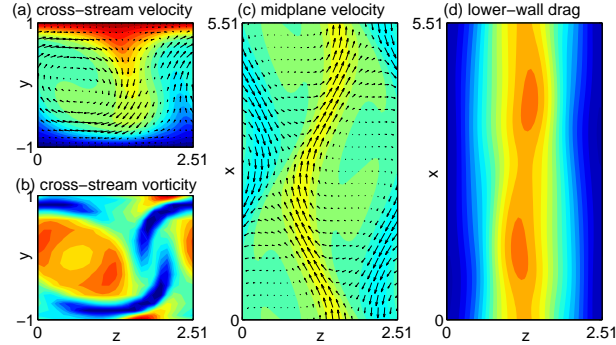


FIGURE 5. \mathbf{u}_{UB} equilibrium: (a) Cross-stream velocity in the $(0, y, z)$ plane, with color indicating (red/blue or light/dark for positive/negative) streamwise (x -direction) flow u , and arrows indicating in-plane flow v, w . (b) Cross-stream vorticity in the same $(0, y, z)$ plane. (c) Velocity in the $(x, 0, z)$ plane midway between the walls at $y = \pm 1$; arrows indicate in-plane velocity u, w ; the color map, streamwise flow u . (d) Drag $\partial u / \partial y$ on the $y = -1$ wall. The color map ranges from near 0 (blue) to 5 times the laminar drag (red). The rolls visible in (a) draw high-speed fluid (red) down from the upper wall, causing a high-speed, high-drag streak in (d), centered at $z = L_z/2$.

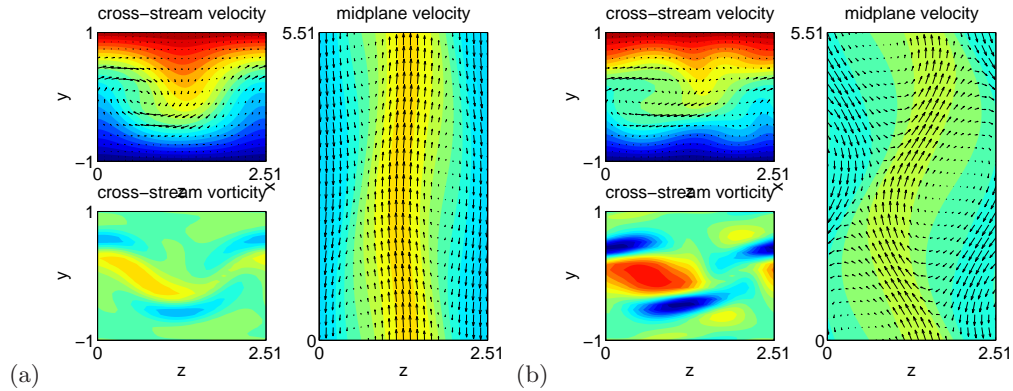


FIGURE 6. (a) \mathbf{u}_{LB} and (b) \mathbf{u}_{NB} equilibria. The subplots are the same as as subplots (a)-(c) in figure 5.

$W_{EQ}^{u,(n)}$ and $W_{EQ}^{u,(n,n+1)}$ are special because they preserve the symmetries shared by the equilibrium and their linear stability eigenvector(s).

The starting point of our unstable / stable manifold explorations are the Waleffe (2003) exact upper-branch and lower-branch equilibria \mathbf{u}_{UB} , \mathbf{u}_{LB} , the new equilibrium \mathbf{u}_{NB} discovered in the course of this investigation, and the corresponding linear stability eigenvalue, eigenfunction pairs λ, \mathbf{v} . We expect the number of equilibria and relative equilibria for any finite cell size to be finite, but we cannot preclude existence of further equilibria or relative equilibria for the plane Couette flow investigated here; the \mathbf{u}_{UB} , \mathbf{u}_{LB} and \mathbf{u}_{NB} equilibria are the only ones found in our numerical Newton searches. All three lie within the fully symmetric subspace \mathcal{U}_s . Their eigenvectors, however, generally do not, and small perturbations carry neighborhoods of these equilibria into the full \mathcal{U} . In what follows, we will mostly focus on dynamics within the \mathcal{U}_s subspace.

Figure 5 shows the upper-branch equilibrium \mathbf{u}_{UB} velocity field and lower-wall drag. Figure 6 shows the velocity field \mathbf{u}_{LB} and a new equilibrium solution of plane Couette flow discovered in the course of this investigation, which we term the \mathbf{u}_{NB} equilibrium

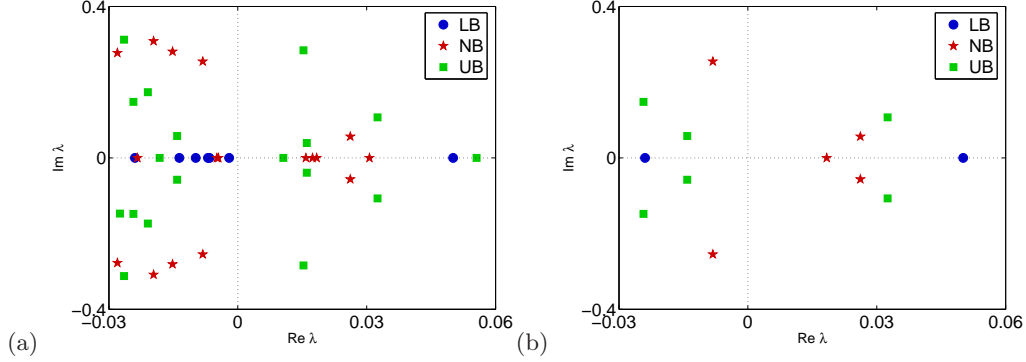


FIGURE 7. Leading \mathbf{u}_{LB} , \mathbf{u}_{NB} , \mathbf{u}_{UB} eigenvalues in (a) the full space \mathbb{U}^{JKL} (b) the symmetric subspace \mathbb{U}_S^{JKL} . For their numerical values, see tables 3 and 4

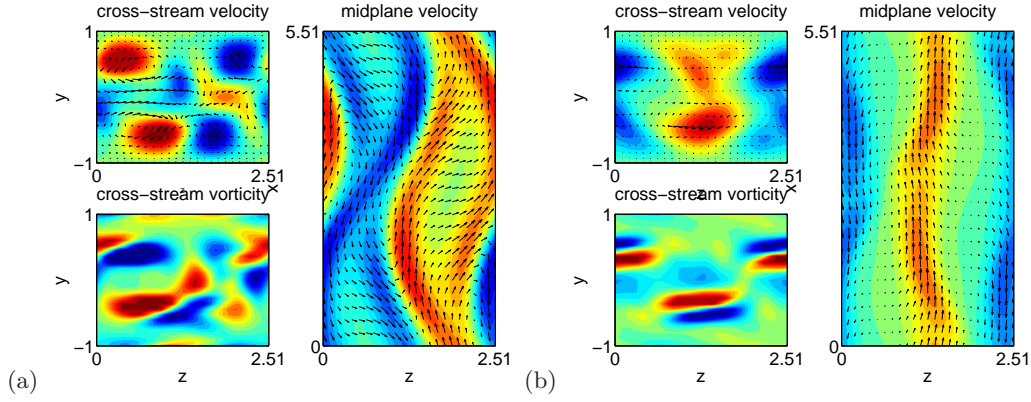


FIGURE 8. Two real-valued superpositions \mathbf{v}^\pm of the complex eigenfunction pair $\mathbf{v}^{(0),(1)}$ corresponding to the unstable complex eigenvalues $\lambda^{(0),(1)}$ of \mathbf{u}_{NB} : (a) \mathbf{v}_{LB}^+ and (b) \mathbf{v}_{LB}^- , see (5.10). Subplots are the same as subplots(a)-(c) in figure 5.

(for “new branch” in keeping with the nomenclature for the other equilibria, pronounced “newbie”). The \mathbf{u}_{NB} equilibrium shown in figure 2 was found via Newton-GMRES search from two different initial guesses: from points along the unstable manifold of the upper-branch, and along the lower-branch.

6. A tour of plane Couette state-space

We now turn to the main theme of this paper: *exact state-space portraiture* of plane Couette flow dynamics, in coordinates systems based on dynamical invariants. Production of state-space portraits requires numerically computed fluid states (e.g. equilibria solutions and their linear stability eigenfunctions), a DNS algorithm, and a method of computing the inner product between fluid states over the domain of the flow (4.3). As we shall now show, this combination of equilibrium solutions, linear stability analysis, and state-space portraiture reveals previously unseen dynamical connections amongst exact coherent states of plane Couette flow. Particularly beautiful and unexpected are the discrete symmetry enforced interrelations between unstable manifolds manifest in figure 2 and figures of this section.

All state-space portraits presented in this section are computed for plane Couette flow for $Re = 400$, $[L_x, L_y, L_z] = [2\pi/1.14, 2, 4\pi/5]$ cell.

6.1. Visualization of ∞ -dimensional state-spaces

Numerical methods have advanced to the point where it is possible to compute highly accurate unstable exact coherent states in turbulent boundary shear flows. How is one to visualize them?

Even though these fully resolved solutions of Navier-Stokes equation are embedded into 10^5+ -dimensional state-space, there are few unstable eigen-directions for moderate Re (close to the onset of turbulence). So, the associated asymptotic strange attractors / repellers might be amenable to dynamical systems visualizations, such as trajectory projections, Poincaré sections, state-space partitions and symbolic dynamics description.

In this section we show that revealing, representation-independent state-space portraits can be defined in terms of invariants of the dynamical system. The idea is to choose a set of characteristic states of the fluid as a basis set, and to project the evolving fluid state $\mathbf{u}(t)$ onto the basis with the inner product (4.3). That is, we choose a set of physically important, linearly independent fluid states $\{\mathbf{e}^{(1)}, \mathbf{e}^{(2)}, \dots, \mathbf{e}^{(n)}, \dots\}$ and produce a state-space trajectory

$$a(t) = (a_1, a_2, \dots, a_n, \dots)(t), \quad a_n(t) = (\mathbf{u}(t), \mathbf{e}^{(n)}) \quad (6.1)$$

in the $\{\mathbf{e}_n\}$ coordinate frame by (4.3). The projection can be viewed in any of the $2d$ planes $\{\mathbf{e}^{(m)}, \mathbf{e}^{(n)}\}$ or in $3d$ perspective views $\{\mathbf{e}^{(\ell)}, \mathbf{e}^{(m)}, \mathbf{e}^{(n)}\}$.

There is an infinity of possible basis sets, but two choices appear particularly natural: A basis can be defined (a) globally, in terms of an equilibrium and its discrete symmetry copies; or (b) locally, in terms of a given equilibrium \mathbf{u}_{EQ} and its linear stability eigenvectors $\mathbf{v}_{\text{EQ}}^{(n)}$. We have found that the dynamic information revealed by one coordinate system often suggests another. These two choices are good starting points.

 6.1.1. A global coordinate frame spanned by τ_i shifts of \mathbf{u}_{EQ}

Define a unit vector $\hat{\mathbf{u}}_{\text{EQ}} = \mathbf{u}_{\text{EQ}} / \|\mathbf{u}_{\text{EQ}}\|$. A set of orthonormal basis vectors for \mathbb{U}_S based on a \mathbf{u}_{EQ} equilibrium and its half-cell translated siblings is then generated from the four irreducible representations of the D_2 dihedral group $\{1, \tau_x, \tau_z, \tau_{xz}\}$ (see §3.2):

$$\begin{array}{l} \mathbf{e}_{\text{EQ}}^{(1)} = \frac{1}{4}(1 + \tau_x + \tau_z + \tau_{xz}) \hat{\mathbf{u}}_{\text{EQ}} \quad \begin{array}{ccc} \tau_x & \tau_z & \tau_{xz} \\ S & S & S \end{array} \\ \mathbf{e}_{\text{EQ}}^{(2)} = \frac{1}{4}(1 + \tau_x - \tau_z - \tau_{xz}) \hat{\mathbf{u}}_{\text{EQ}} \quad \begin{array}{ccc} S & A & A \\ \mathbf{e}_{\text{EQ}}^{(3)} = \frac{1}{4}(1 - \tau_x + \tau_z - \tau_{xz}) \hat{\mathbf{u}}_{\text{EQ}} \quad \begin{array}{ccc} A & S & A \\ \mathbf{e}_{\text{EQ}}^{(4)} = \frac{1}{4}(1 - \tau_x - \tau_z + \tau_{xz}) \hat{\mathbf{u}}_{\text{EQ}} \quad \begin{array}{ccc} A & A & S \end{array} \end{array} \end{array} \quad (6.2)$$

where the last 3 columns refer to the symmetry of the \mathbf{u} projection under half-cell translations. (We shall omit the equilibrium label whenever we can, $\mathbf{e}_{\text{EQ}}^{(j)} \rightarrow \mathbf{e}^{(j)}$). Like the equilibrium state from which they are constructed, these basis elements are fluid states in \mathbb{U} , vector-valued time-independent functions of the (x, y, z) spatial coordinates of the flow over the cell domain Ω .

As the “velocity” \mathbf{u} in the Navier-Stokes equation (3.1) for plane Couette flow is the deviation from laminar flow, the origin in state-space portraits corresponds to the laminar equilibrium \mathbf{u}_{LM} . This origin is shared by all symmetry invariant subspaces, as \mathbf{u}_{LM} is invariant under all symmetries of the flow.

6.1.2. A local coordinate frame spanned by \mathbf{u}_{E_Q} eigenfunctions

The eigenfunctions of an equilibrium provide a good coordinate system for viewing its local dynamics. Since \mathbf{u} is real-valued, all eigenvalues are real-valued or complex pairs. The eigenfunction \mathbf{v} of a real eigenvalue spans a line in \mathbb{U} , and the real-valued superpositions \mathbf{v}^\pm (5.10) of a complex pair span a plane in \mathbb{U} . A real-valued orthogonal coordinate system that spans the unstable modes of an equilibrium can be constructed by Gram-Schmidt orthogonalizing the corresponding set of real-valued fields, e.g. $\{\mathbf{v}^{(1)}, \mathbf{v}^{+(2,3)}, \mathbf{v}^{-(2,3)}\}$ for an equilibrium with unstable eigenvalues $\lambda^{(1)} \in \mathbb{R}$ and $\lambda^{(2)} = \lambda^{(3)*} \in \mathbb{C}$.

6.2. A global stroll through plane Couette flow state-space

With the above road maps in hand, let us take a stroll through the state-space of a transiently turbulent plane Couette flow. As so many dynamical narratives, this will be a long walk through unfamiliar landscape with many landmarks of local interest. We undertake the tour for several reasons: (1) The main message is that now such a promenade is possible even in 10^5 dimensions. But a detailed road map is a necessary step in solving at least two outstanding problems: (2) a state-space partition is a prerequisite for a systematic exploration of dynamical invariant structures such as relative periodic orbits, and (3) explicit linear stability eigenvectors and their unstable-manifold continuations will be needed to control and chaperone a given fluid state to a desired target state.

To keep things simple, for the remainder of this tour we focus only on the S -symmetric subspace \mathbb{U}_S . As noted in § 5, \mathbf{u}_{LB} , \mathbf{u}_{NB} , and \mathbf{u}_{UB} and their half-cell translations lie within \mathbb{U}_S . We form the global coordinate frame (6.2)

$$\{\mathbf{e}_{UB}^{(1)}, \mathbf{e}_{UB}^{(2)}, \mathbf{e}_{UB}^{(3)}, \mathbf{e}_{UB}^{(4)}\} \quad (6.3)$$

from the upper-branch equilibrium \mathbf{u}_{UB} and its three half-cell translated siblings. The evolution of a state $\mathbf{u} \in \mathbb{U}_S$ is represented in this coordinate frame by the trajectory $a(t) = (a_1, a_2, a_3, a_4)(t)$ (6.1).

Our first example of a global state-space portrait of plane Couette flow is figure 2. Here trajectories in the unstable manifolds of \mathbf{u}_{LB} , \mathbf{u}_{NB} , \mathbf{u}_{UB} and several of their half-cell translations are projected onto the $\{\mathbf{e}^{(1)}, \mathbf{e}^{(2)}\}$ plane, as defined by (6.2) for the \mathbf{u}_{UB} equilibrium. Both $\mathbf{e}^{(1)}$ and $\mathbf{e}^{(2)}$ are symmetric in τ_x , so points that are related by half-cell translations in x (such as \mathbf{u}_{LB} and $\tau_x \mathbf{u}_{LB}$) map to the same point in this projection. $\mathbf{e}^{(1)}$ is antisymmetric in τ_z , so half-cell translations in z appear symmetrically opposite about $a_2 = 0$.

The \mathbf{u}_{LB} unstable manifold W_{LB}^u forms the backbone of the dynamics shown in Figure 2. The \mathbf{u}_{LB} equilibrium has a single real-valued unstable eigenvalue, as shown in figure 7 and discussed in detail in Wang *et al.* (2007). W_{LB}^u is therefore $1d$ and can be calculated in its entirety as discussed in § 5.2. Figure 2 shows the projection of W_{LB}^u onto $\{\mathbf{e}^{(1)}, \mathbf{e}^{(2)}\}$ plotted with thick blue lines. One branch of W_{LB}^u decays immediately to laminar flow. The \mathbf{u}_{LB} state has large components of the first even Stokes mode and two heat modes, $(k_y, k_z) = (1, 1)$ and $(k_y, k_z) = (2, 0)$. These eigenfunctions of laminar flow have close but unequal eigenvalues; hence the curvature in the path from \mathbf{u}_{LB} to \mathbf{u}_{LM} in Figure 2. The other branch grows away from laminar flow and takes a transient turbulent excursion towards \mathbf{u}_{UB} . The unstable manifold of $\tau_z \mathbf{u}_{LB}$ was obtained by applying the τ_z translation to W_{LB}^u .

The \mathbf{u}_{NB} unstable manifold W_{NB}^u : Within \mathbb{U}_S , the \mathbf{u}_{NB} equilibrium has a complex pair of unstable eigenvalues and one real unstable eigenvalue (figure 7). The instability of the real eigenvalue is weaker than the complex pair; we omit it from consideration here

and focus on the $2d$ subset $W_{\text{NB}}^{u,(1,2)}$ corresponding to the complex pair $\lambda_{\text{NB}}^{(1,2)}$. $W_{\text{NB}}^{u,(1,2)}$ is shown in figure 2 as a spiral of trajectories emanating from \mathbf{u}_{NB} , calculated as discussed in §5.2. This simple geometric picture produces our first striking result: the $2d$ surface $W_{\text{NB}}^{u,(1,2)}$ is apparently bounded by the $1d$ curve $W_{\text{NB}}^{u,(1,2)}$.

A heteroclinic connection from \mathbf{u}_{NB} to \mathbf{u}_{LB} : As it approaches \mathbf{u}_{LB} , $W_{\text{NB}}^{u,(1,2)}$ separates along the two branches of W_{LB}^u . Since \mathbf{u}_{LB} has a single unstable eigenvalue, we expect that a single trajectory in $W_{\text{NB}}^{u,(1,2)}$ straddles the split along W_{LB}^u and is drawn in towards \mathbf{u}_{LB} along the stable eigenvectors as $t \rightarrow \infty$, forming a heteroclinic connection from \mathbf{u}_{NB} to \mathbf{u}_{LB} .

This is a strikingly unexpected result. In dimensions higher than two, heteroclinic connections are nongeneric, since it is unusual that a $1d$ trajectory can be arranged to strike a particular zero-dimensional point. However, discrete symmetries and the dimensionality of the \mathbf{u}_{LB} unstable manifold make heteroclinic connections possible here (Kevrekidis *et al.* (1990); Holmes *et al.* (1996); Cvitanović *et al.* (2007)). The set of candidate trajectories emerging from the neighborhood of \mathbf{u}_{NB} is increased from one dimension to two by the complex instability (or three if $\lambda_{\text{NB}}^{(3)}$ is considered as well). The dimensionality of state space near the target \mathbf{u}_{LB} is effectively reduced to one by its codimension-1 set of stable eigenvalues.

Considered in the full, nonsymmetric space \mathbb{U} , the continuous translation symmetry increases the dimensionality of both the candidate trajectories and the target by two. However, the invariance of \mathbb{U}_S under Navier-Stokes immediately restricts possible heteroclinic connections between the torus of \mathbf{u}_{NB} and \mathbf{u}_{LB} translations to those with the same phase of S symmetry. For example, if a trajectory in the unstable manifold of \mathbf{u}_{LB} terminates at a \mathbf{u}_{LB} state, it may do so at only the \mathbf{u}_{LB} translations within \mathbb{U}_S , namely $\mathbf{u}_{\text{LB}}, \tau_x \mathbf{u}_{\text{LB}}, \tau_z \mathbf{u}_{\text{LB}}$, or $\tau_{xz} \mathbf{u}_{\text{LB}}$.

Note also that most weakly stable eigenvalues of \mathbf{u}_{LB} , $\lambda_{\text{UB}}^{(4)}$ through $\lambda_{\text{UB}}^{(8)}$, are outside the \mathbb{U}_S subspace, so trajectories in $W_{\text{NB}}^{u,(1,2)}$ are forced to approach \mathbf{u}_{LB} along the more strongly contracting eigendirections of $\lambda_{\text{UB}}^{(9)}$ and $\lambda_{\text{UB}}^{(10)}$ (table 3).

The heteroclinic connection forms a boundary between trajectories that decay immediately to laminar flow and those that grow towards transient turbulence. Those that pass near \mathbf{u}_{LB} and grow to turbulence follow the unstable manifold of \mathbf{u}_{LB} into a region near the \mathbf{u}_{UB} equilibrium. For these parameters, all generic initial conditions investigated so far ultimately decay to laminar. But, at higher Reynolds numbers and larger geometries for which turbulence is sustained, we expect the heteroclinic connection will form a $1d$ portion of the boundary of the laminar state's basin of attraction. This $1d$ boundary should be extendable to $2d$ by adding the second unstable eigenvalue of \mathbf{u}_{NB} into consideration.

Lastly, we note that the $\{\mathbf{e}_1, \mathbf{e}_2\}$ plane of projection in figure 2 is symmetric in τ_x , so any two points \mathbf{u} and $\tau_x \mathbf{u}$ are mapped to the same point in the projection. Thus, it is not possible to determine from figure 2 alone whether the heteroclinic connection from \mathbf{u}_{NB} goes to \mathbf{u}_{LB} or $\tau_x \mathbf{u}_{\text{LB}}$. In figure 9, we add a third, τ_x -antisymmetric coordinate to the perspective to distinguish these points and show that the heteroclinic connection is towards \mathbf{u}_{LB} .

Heteroclinic connection from \mathbf{u}_{NB} to $\tau_{xz} \mathbf{u}_{\text{LB}}$: A second, similar separation of $W_{\text{NB}}^{u,(1,2)}$ occurs in the bottom half of figure 2, near the τ_z translation of \mathbf{u}_{LB} . Trajectories on the laminar side of $\tau_z \mathbf{u}_{\text{LB}}$ follow its unstable manifold towards the laminar state; those on the other side head towards turbulence along the other branch of the $\tau_z \mathbf{u}_{\text{LB}}$ unstable manifold. As mentioned previously, the τ_x -symmetric projection of figure 2 maps $\tau_z \mathbf{u}_{\text{LB}}$ and $\tau_{xz} \mathbf{u}_{\text{LB}}$ to the same point (marked $\tau_z \mathbf{u}_{\text{LB}}$ in the figure), so additional information

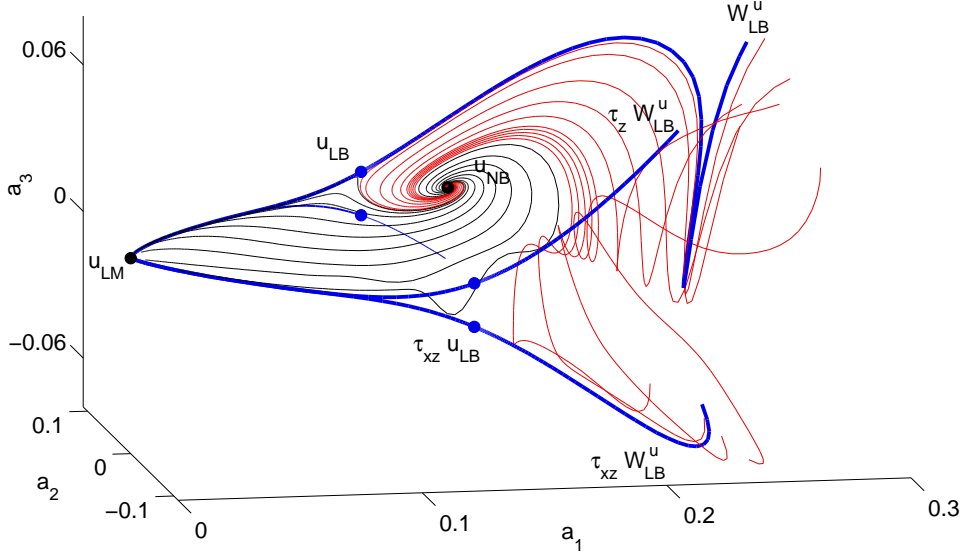


FIGURE 9. Unstable manifolds of \mathbf{u}_{LB} and its half-cell translations, and a 2d portion of the \mathbf{u}_{NB} unstable manifold, projected from 61,506 dimensions to 3 in the \mathbf{u}_{UB} global basis (6.3).

is needed to determine which of these two states is the endpoint of the heteroclinic connection from \mathbf{u}_{NB} .

The states can be distinguished by adding a τ_x -antisymmetric coordinate to the projection. Figure 9 shows a 3d perspective obtained by adding $a_3 = (\mathbf{u}, \mathbf{e}^{(3)})$ to the 2d projection of figure 2. The added perspective shows that the second division in $W_{NB}^{u,(1,2)}$ is due to $W_{\tau_{xz}NB}^u = \tau_{xz} W_{NB}^u$, the unstable manifold of $\tau_{xz}\mathbf{u}_{LB}$. Trajectories in $W_{NB}^{u,(1,2)}$ falling on one side of $\tau_{xz}\mathbf{u}_{LB}$ follow one branch of $\tau_{xz}W_{LB}^u$ to the laminar state; those on the other side follow the other branch towards \mathbf{u}_{UB} .

The geometry of $W_{NB}^{u,(1,2)}$ in this region is fairly complex. Different portions of it are guided by the unstable manifolds of $\tau_{xz}\mathbf{u}_{LB}$, $\tau_z\mathbf{u}_{LB}$, and \mathbf{u}_{LB} . Figure 9 also shows that a portion of $W_{NB}^{u,(1,2)}$ is drawn towards $\tau_z\mathbf{u}_{UB}$ and is guided by its unstable manifold.

Thus, with two simple state-space portraits, we have identified several regions in state-space that trigger transitions toward qualitatively different types of flow (and each of these regions is multiplied by four by the discrete symmetries). We expect that identification of such “trigger regions” and their stability modes will be extremely valuable in the development of nonlinear control strategies for wall-bounded shear flows.

6.3. Local state-space portraits: the unstable manifold of \mathbf{u}_{UB} in \mathbb{U}_S

Figure 10 shows the unstable manifold of \mathbf{u}_{UB} within \mathbb{U}_s , in a \mathbf{u}_{UB} -centric 3d perspective plot. The \mathbf{u}_{UB} has a single complex pair of unstable eigenvalues $\lambda^{(1)} = \lambda^{(2)*}$ in \mathbb{U}_s , forming a 2d unstable manifold, $W_{UB}^{u,S}$, within this symmetric subspace. The basis set $\{\mathbf{e}^{(1)}, \mathbf{e}^{(2)}, \mathbf{e}^{(3)}\}$ for the 3d perspective of figure 10 is a Gram-Schmidt orthogonalization of the plane of oscillation, given by $\mathbf{v}_{UB}^{\pm,(1,2)}$, and the direction of the initial departure from the linear dynamics, given by $(\mathbf{u}_B - \mathbf{u}_A)$. Since there are only two unstable eigenvalues in \mathbb{U}_S , this choice for a third coordinate for the local basis provides a convenient view into the transition from linear to nonlinear dynamics.

Figure 10(a) shows $W_{UB}^{u,S}$ originating as an outward spiral in the plane of $\mathbf{v}_{UB}^{\pm,(1,2)}$. Strong nonlinearity and strong trajectory separation first occurs near point A: on the

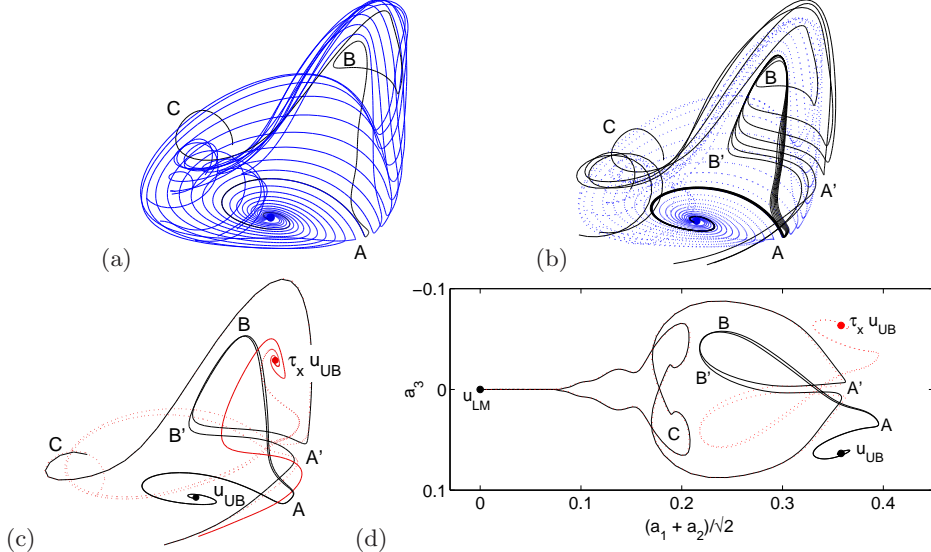


FIGURE 10. (a) A perspective view of $W_{\mathbf{u}_{\text{UB}}}^{u,S}$, the unstable manifold of the \mathbf{u}_{UB} equilibrium within the \mathbb{U}_S symmetric subspace. (b) A refined view of dynamics within $W_{\mathbf{u}_{\text{UB}}}^{u,S}$. (c) A pair of nearby trajectories from the refined view of (b) plotted against trajectories in the unstable manifold of $\tau_x \mathbf{u}_{\text{UB}}$. The dotted trajectories spiraling out of $\tau_x \mathbf{u}_{\text{UB}}$ are the τ_x translations of the solid trajectories spiraling out of \mathbf{u}_{UB} . The $3d$ perspective for these plots spans the plane of \mathbf{u}_{UB} 's unstable complex pair and the upward direction of the trajectory at A . (d) The symmetric trajectories of (c) replotted in translation-symmetric coordinates.

left of A , trajectories continue the unstable linear oscillation for another cycle; on the right, they follow distinctly different dynamics.

Figure 10 (b) shows a refinement of $W_{\mathbf{u}_{\text{UB}}}^{u,S}$ on one side of the split at A . The refined trajectories undergo a second separation from their neighbors in figure 10 (a), occurring between B and B' , and a third separation among themselves at A' . The separation at A' is notably similar to the first separation at A : the portion of $W_{\mathbf{u}_{\text{UB}}}^{u,S}$ on the left of A' continues with apparently unchanged curvature; the portion on the right shoots up from A' , around B , and down towards C in the same manner as the initial split at A in figure 10 (a).

Figure 10 (c) suggests that separations of $W_{\mathbf{u}_{\text{UB}}}^{u,S}$ at A and A' and its subsequent curvature around B are due to the influence of its τ_x -symmetric counterpart, $W_{\tau_x \mathbf{u}_{\text{UB}}}^{u,S} = \tau_x W_{\mathbf{u}_{\text{UB}}}^{u,S}$. Figure 10 (b) shows the two trajectories in $W_{\mathbf{u}_{\text{UB}}}^{u,S}$ that straddle the split at A' in figure 10 (a) and their τ_x -symmetric counterparts in $\tau_x W_{\mathbf{u}_{\text{UB}}}^{u,S}$, projected into the same perspective as figure 10 (a) and (b). The arc of the $W_{\mathbf{u}_{\text{UB}}}^{u,S}$ trajectories from A to B and from A' over B to C is parallel to the initial linear oscillation around $\tau_x \mathbf{u}_{\text{UB}}$. Note that the two pairs of trajectories in $W_{\mathbf{u}_{\text{UB}}}^{u,S}$ and $\tau_x W_{\mathbf{u}_{\text{UB}}}^{u,S}$ draw together just before A' . The pairs split at A' and exchange allegiance, so that past A' , trajectories on opposite unstable manifolds follow almost identical paths.

Dynamics within the \mathbb{U}_S unstable manifolds of \mathbf{u}_{UB} and $\tau_x \mathbf{u}_{\text{UB}}$ thus appears to be composed, at least initially, of chaotic alternation between unstable oscillations around a pair of symmetric equilibria, in a manner reminiscent of the Lorenz system. For the parameters of this study, the trajectories investigated so far leave the region of the \mathbf{u}_{UB} and its translations after a few oscillations, so that the \mathbf{u}_{UB} unstable manifold has the characteristics of a chaotic repeller. We expect that that periodic orbits can be found

in this region and that chaotic dynamics are sustained at higher Reynolds numbers and larger geometries.

A translation-symmetric view of the \mathbf{u}_{UB} and $\tau_x \mathbf{u}_{\text{UB}}$ unstable manifolds: Further insight to the interplay between $W_{\text{UB}}^{u,S}$ and $\tau_x W_{\text{UB}}^{u,S}$ can be obtained by replotting in a translation-symmetric basis. Figure 10(d) shows the pairs of nearby trajectories in $W_{\text{UB}}^{u,S}$ and $\tau_x W_{\text{UB}}^{u,S}$ shown in figure 10(c). The projection is onto the global, symmetric coordinates $(\mathbf{e}^{(1)} + \mathbf{e}^{(2)})/\sqrt{2} = \frac{1}{2\sqrt{2}}(1 + \tau_x) \hat{\mathbf{u}}_{\text{UB}}$, and $\mathbf{e}^{(3)}$ as defined in (6.2). These basis vectors are symmetric and antisymmetric in τ_x . The first was chosen because it provides a clear view of the path $ABB'A'$. The τ_x -antisymmetric long-term behavior of two nearby initial conditions from \mathbf{u}_{UB} suggests that the path from B' to A' is one of weakening x variation, reaching small but nearly τ_x -antisymmetric x variation near A' . After A' , a τ_x -antisymmetric instability in x -variation kicks in, resulting in long-term τ_x -antisymmetric dynamics.

6.4. Transient turbulence

The final stop in our stroll through plane Couette state space is an illustration of transient turbulence against the backdrop of the invariant structures featured in previous figures. Figure 11(a) shows a single trajectory, initiated as a perturbation of \mathbf{u}_{NB} , that exhibits transient turbulence and then decays to laminar flow. The region of state-space explored by this trajectory is typical of all observed transiently turbulent dynamics in the \mathbb{U}_S symmetric subspace. The trajectory is unusually long-lived; it wanders for some 1000 time units before converging on the laminar state, compared to more typical 200 time unit lifetimes of the trajectories in figure 10(d).

When seen in isolation, the turbulent trajectory shows little discernable order. When plotted within the framework of invariant structures of the flow, in figure 11(b), structure is immediately evident. In this 3d perspective, the decay to laminar flow is confined to a region bounded by the \mathbf{u}_{NB} and \mathbf{u}_{LB} unstable manifolds. Transient turbulence occurs on the far side of laminar from these states, $a_1 > 0.15$, and in a region shaped roughly by the unstable manifolds of \mathbf{u}_{LB} , \mathbf{u}_{UB} , \mathbf{u}_{NB} , and their half-box translations. Close inspection shows that portions of the transient turbulent trajectory follow the contours of nearby unstable manifolds.

7. Conclusion and perspectives

Currently a large conceptual gap separates what has been achieved for low-dimensional dynamical systems and the challenges we face in understanding infinite-dimensional turbulent flows. The detailed dynamical information measured in experiments, and its agreement with the qualitative features of the full Navier-Stokes DNS offer a hope that a dynamical theory of moderate Re numbers turbulence is within reach.

Motivated by the recent observations of recurrent coherent states in experiments and numerical studies (reviewed in §2), we initiate here a systematic exploration of the hierarchy of exact unstable invariant solutions of fully-resolved Navier-Stokes equations in order to describe the spatio-temporally chaotic dynamics of turbulent fluid flows. At first glance, turbulent dynamics visualized in the state-space might appear hopelessly complex, but under a detailed examination it appears much less so than feared: it is pieced together from exact coherent states connected by fast transient interludes. Plane Couette flow equilibria, relative equilibria and periodic solutions embody Hopf's vision: repertoire of recurrent spatio-temporal patterns explored by turbulent dynamics. We visualize turbulence as a walk through a repertoire of unstable recurrent patterns. As a turbulent flow evolves, every so often we catch a glimpse of a familiar pattern. For any finite spatial

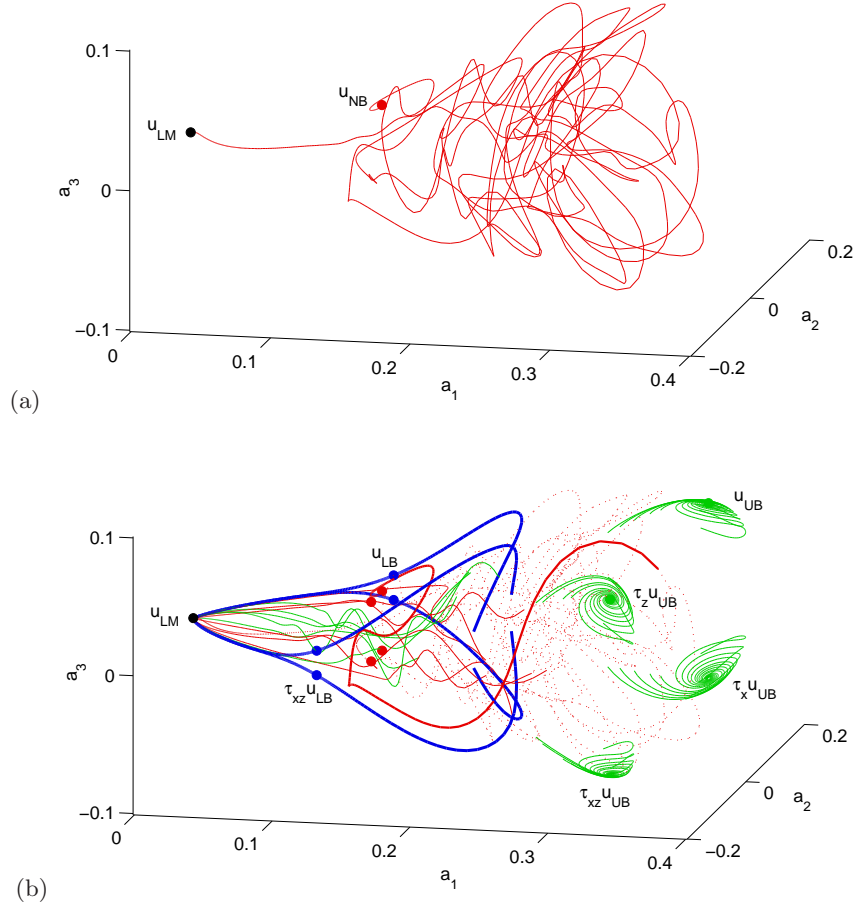


FIGURE 11. **A transiently turbulent trajectory** in the \mathbf{u}_{NB} unstable manifold, (a) in isolation (b) in relation to \mathbf{u}_{LB} , \mathbf{u}_{NB} , \mathbf{u}_{UB} , their half-cell translations, and their unstable manifolds. The final decay to laminar of several other trajectories in the unstable manifolds of \mathbf{u}_{NB} and \mathbf{u}_{UB} are also shown.

resolution, the flow approximately follows for a finite time a pattern belonging to a finite alphabet of admissible fluid states, represented here by a set of exact coherent states.

What new insights does the “unstable coherent states program” offer? Normal form models derived from severe truncations of spectral representations of PDEs - most famously the Lorenz model - capture *qualitatively* the bifurcations and chaotic dynamics evocative of those observed in fluid dynamics. In contrast, the exact unstable coherent states / periodic orbit theory provide accurate *quantitative* predictions for 3D Navier-Stokes dynamical observables (such as the average turbulent drag), for a given flow, given flow geometry, given Re and other parameters. This description should lead to quantitative predictions of transport properties of fluid flows such as bulk flow rate, mean wall drag, and their fluctuations. Ability to compute the exact unstable eigenfunctions such as the pair is plotted (8) opens a new approach to control of boundary shear turbulence; applied as a perturbation to the 3D flow they can be used to stabilize or chaperone the flow towards a desired fluid state, and not necessarily the laminar one.

The state-space exploration of equilibria and their global unstable manifolds presented in here is the first step. While important in organizing the turbulent flow, equilibria, being static, do not actually participate in it. That role is played by the infinity of unstable periodic orbits densely embedded in the asymptotic attractor. That it is possible to compute exact unstable periodic solutions of 3D Navier-Stokes has been demonstrated in the pioneering work of Kawahara & Kida (2001), for periodic orbits, and Viswanath (2007b), for relative periodic orbits. However, a combination of novel and proven numerical and analytical techniques such as variational solvers, periodic orbit theory, and group representation theory still needs to be developed in order to systematically explore the hierarchy of such solutions, and apply Cvitanović *et al.* (2006) periodic orbit theory to calculation of quantitative predictions for 3D Navier-Stokes dynamical observables.

Another outstanding issue that has to be addressed in future work, is that in computations spanwise-streamwise periodic cells are chosen just sufficiently large to observe the empirically observed sustained turbulence. Such small cells introduce dynamical artifacts such as lack of structural stability, cell-size dependence of the sustained turbulence states, and boundary-condition dependent coherent states unlike those observed in large aspect ratio experiments.

We would like to acknowledge D. Viswanath's patient advice essential to the linearized stability calculations reported here. F.W. was supported in part by NSF grant number GR/F/12345. P.C. and J.F.G. thank G. Robinson, Jr. for support. J.H. thanks R. Mainieri for partial support.

Appendix A. Numerical methods

A.1. CFD algorithm

Our CFD algorithm is an implementation of the velocity-pressure algorithm of Kleiser & Schuman (1980), with the velocity field expanded as in (4.17). Real-valuedness of \mathbf{u} implies $\hat{u}_{j,-k,l,m} = \hat{u}_{-j,k,l,m}^*$, so only coefficients with $k \geq 0$ are stored. Time-stepping is performed with finite-differencing, boundary conditions are enforced with a Chebyshev tau method, and incompressibility is enforced through influence-matrix method and tau-correction methods (Canuto *et al.* (1988)). Unless otherwise noted, our simulations are performed with rotational evaluation of the nonlinear term, 3rd-order semi-implicit backwards-differentiation time-stepping (Peyret (2002)) with 2nd-order Runge-Kutta initialization (Spalart *et al.* (1990)), a variable time-step with CFL number bounded between 0.4 and 0.6 (resulting in $\Delta t \approx 0.025$), full dealiasing in x, z , and a $32 \times 35 \times 32$ grid after dealiasing. We zero the highest-order cosine modes of the discrete Fourier transform (Trefethen (2000)), and our spectral discretization (4.17) is $(J, K, L) = (15, 34, 15)$ (for comparison, the resolution of equilibria computed in Waleffe (2003) was $(J, K, L) = (11, 23, 11)$). We show in § B that this resolution is sufficient and highly accurate for the problem at hand.

We have verified the correctness of our DNS algorithm with a test suite of known solutions for the main components of the algorithm and against several known solutions for DNS as a whole, including Orr-Sommerfeld eigenfunctions, sinusoidal perturbations to the mean flow, Waleffe (2003) equilibrium solutions and their eigenvalues within the S -symmetric subspace \mathbb{U}_S , and several plane Couette flow periodic orbits determined by Viswanath (2007b). All computations in this study were performed with **Channelflow**. They provide a fully independent verification of the existence and high numerical accuracy of exact coherent states found by Waleffe (2003) and Viswanath (2007b). **Channelflow** is a high-level software library for numerical computation in channel geometries written and maintained by Gibson (2007), available for free download

at Channelflow.org. `Channelflow` uses `FFTW` for Fourier transforms (Frigo & Johnson (2005)), specialized banded matrix routines for solution of linear time-stepping equations, `LAPACK` for general-purpose linear algebra (Anderson *et al.* (1999)), and the `Octave` libraries (Eaton (2007)) for a high-level interface to `LAPACK`.

The basis elements Φ_n are represented numerically with Chebyshev expansions for their y -variation, so the sum $\mathbf{u} = \sum_{n=1}^d a_n \Phi_n$ is computed by adding the Chebyshev coefficients of $a_n \Phi_n$ to the appropriate modes of the \mathbf{u} CFD expansion (4.17). The L^2 inner product $a_n = (\mathbf{u}, \Phi_n)$ is orthogonal in the Fourier modes and requires only one evaluation of a $1d$ integral in y . Our code uses an exact N_y^2 computation of the y -integral, though a faster quadrature integration would be adequate. The computational overhead associated with conversion between the state-space and CFD representations is negligible compared to the overall cost of integrating the CFD algorithm in time.

A.2. Determination of equilibria with Newton-GMRES

The upper-branch and lower-branch equilibria were obtained in Waleffe (2003) by a continuation method. The starting state was a streaky flow with weak counter-rotating rolls sustained by a weak artificial body force. The algorithm employed a velocity-vorticity formulation of Navier-Stokes, evaluation of the Newton-step equations through numerical differentiation of the linearized equations for the expansion coefficients, and solution of the resulting equations through direct linear algebra methods. The size of the linear algebra problems was kept manageable by staying within the S -symmetric subspace \mathbb{U}_S and employing an elliptical truncation in (4.17) that zeroed modes with

$$\hat{u}_{jklm} = 0 \quad \text{for } j^2/(J+1)^2 + k^2/(K+1)^2 + l^2/(L+1)^2 \geq 1. \quad (\text{A } 1)$$

Viswanath (2007b) has taken such computations to much higher-dimensional spaces (excess of 10^5) by using Krylov-subspace methods. GMRES (Generalized Minimum Residual) is a Krylov-subspace method for solving linear algebra problems of the form $Ax = b$ repeated evaluations with $A\hat{x}$ for test vectors \hat{x} (Trefethen & Bau (1997)). Only products $A\hat{x}$ are required for the algorithm, not the matrix A itself. If A is dominated by a few large eigenvalues, Krylov methods can converge very rapidly. Viswanath found that 10^5 -dimensional Newton equations for solutions of moderate- Re , small aspect ratio plane Couette flow typically converge to 10^{-3} accuracy within 30 iterations, thus allowing for the increase in state-space dimensionality needed to determine periodic orbits and relative periodic orbits.

We adapted the Newton-Krylov method to the state-space representation outlined in §4 as follows. An equilibrium \mathbf{u}_{EQ} of plane Couette flow satisfies $\mathbf{u}_{\text{EQ}} = f_{\text{CFD}}^T(\mathbf{u}_{\text{EQ}})$ for any $T > 0$, or, in the state-space representation, $a_{\text{EQ}} = f^T(a_{\text{EQ}})$. For a point a near an equilibrium solution a_{EQ} , we seek a Newton step Δa such that $a_{\text{EQ}} = a + \Delta a$ by linearizing $a + \Delta a = f^T(a + \Delta a)$ about a and solving for Δa , *i.e.*,

$$(I - Df^T|_a) \Delta a = a - f^T(a) \quad (\text{A } 2)$$

where Df is the Jacobian (4.8). If the search is performed in a space that retains the continuous translation symmetries, additional constraints are necessary to prevent Δa variations along symmetry directions. Viswanath (2007b) adds to the Newton step (A 2) two equations enforcing that Δa is orthogonal to the the x and z translation directions,

$$\sum_{n=1}^d \left(\frac{\partial \mathbf{u}}{\partial x}, \Phi_n \right) \Delta a_n = 0, \quad \sum_{n=1}^d \left(\frac{\partial \mathbf{u}}{\partial z}, \Phi_n \right) \Delta a_n = 0.$$

Solution of the set of Newton equations via GMRES requires repeated evaluation of the

(N_x, N_y, N_z)	(J, K, L)	truncation	$\ \partial \mathbf{u}_{\text{UB}}/\partial t\ $
(24, 24, 24)	(11, 23, 11)	elliptical	$5 \cdot 10^{-4}$
(32, 35, 32)	(15, 34, 15)	rectangular	$3 \cdot 10^{-5}$
(48, 49, 48)	(23, 48, 23)	rectangular	$5 \cdot 10^{-7}$
(48, 65, 48)	(23, 64, 23)	rectangular	$3 \cdot 10^{-9}$

TABLE 2. Precision of \mathbf{u}_{UB} equilibrium calculation with different spectral resolutions. The time derivatives were estimated with one step of a 2nd-order semi-implicit Runge-Kutta algorithm and skew-symmetric computation of the nonlinear terms. $\|\cdot\|$ is the inner product (4.3) norm.

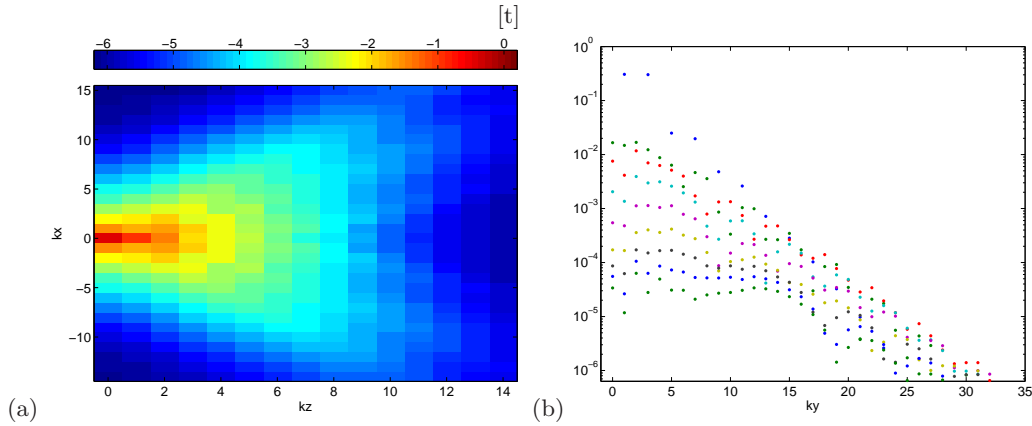


FIGURE 12. Spectral resolution of the \mathbf{u}_{UB} equilibrium: (a) Fourier spectrum: The color(grayscale) map shows $\frac{1}{2} \log_{10} \left| \int_{-1}^1 \hat{\mathbf{u}}_{j\ell}(y) \cdot \hat{\mathbf{u}}_{j\ell}^*(y) dy \right|$ as a function of k_j, k_ℓ . (b) Chebyshev spectrum: $|\hat{u}_{jk\ell}| + |\hat{v}_{jk\ell}| + |\hat{w}_{jk\ell}|$ is plotted versus ℓ for $j = k = 0, 1, 2, \dots$

constraint equations and the linear product $(I - Df^T|_a) \Delta \hat{a}$ for equilibrium guesses $\Delta \hat{a}$. We approximate these products with a CFD algorithm by

$$[(I - Df^T|_a) \Delta \hat{a}]_m = a_m - \frac{1}{\epsilon} (f_{\text{CFD}}^T(\mathbf{u} + \epsilon \Delta \hat{\mathbf{u}}) - f_{\text{CFD}}^T(\mathbf{u}, \Phi_m)) + O(\epsilon), \quad (\text{A } 3)$$

where $\Delta \hat{\mathbf{u}} = \sum_{n=1}^d \Delta \hat{a}_n \Phi_n$. The right-hand side of (A 2) and the accuracy of the equilibrium condition (5.2) are also evaluated by CFD:

$$\begin{aligned} [a - f^T(a)]_m &= (\mathbf{u} - f_{\text{CFD}}^T(\mathbf{u}, \Phi_m)) \\ \frac{\partial \mathbf{u}_{\text{EQ}}}{\partial t} &= \frac{1}{\Delta t} (f_{\text{CFD}}^{\Delta t}(\mathbf{u}_{\text{EQ}}) - \mathbf{u}_{\text{EQ}}). \end{aligned} \quad (\text{A } 4)$$

The integration time T is a free parameter which must be chosen to balance the cost of computing $f^T(a)$, which increases with T , against the improved convergence of GMRES iteration due to better separation of the eigenvalues of $(I - Df^T|_a)$ as T increases. For our calculations an integration time of $T = 10$ was found to provide a good balance.

We used Newton-GMRES to refine the Waleffe (2003) equilibria from $(J, K, L) = (11, 23, 11)$ with the elliptical truncation (A 1) to $(J, K, L) = (15, 35, 15)$ and $(24, 49, 24)$ with rectangular spectral truncation $|j| \leq J, |k| \leq K, 0 \leq \ell \leq L$. In each case the residual of the equilibrium condition was reduced to 10^{-14} within a few Newton steps, resulting in equilibria \mathbf{u}_{EQ} for which $\|\partial \mathbf{u}_{\text{EQ}}/\partial t\| \approx 10^{-14}$ as well. This precision, however, exceeds the precision of the CFD algorithm with which the solutions were calculated.

An estimate of the accuracy of the solutions is obtained by computing $\|\partial \mathbf{u}_{\text{EQ}}/\partial t\|$ with a different choices for the CFD algorithm and parameters. We found that the accuracy of the computation was limited by aliasing errors in the y -transforms, which are affected the method of evaluation of the nonlinear term $\mathbf{u} \cdot \nabla \mathbf{u}$. Switching from the rotational form $(\nabla \times \mathbf{u}) \times \mathbf{u}$, which we used in the Newton-GMRES iteration for its speed, to the skew-symmetric form $\frac{1}{2} \mathbf{u} \cdot \nabla \mathbf{u} + \frac{1}{2} \nabla(\mathbf{u} \cdot \mathbf{u})$, increased the norm of the time-derivatives to the values shown in table 2. We take these norms to indicate the numerical precision of the equilibrium solutions computed here.

Figure 12 shows Fourier and Chebyshev spectra for the \mathbf{u}_{UB} computed at resolution $(J, K, L) = (15, 34, 15)$ on a $32 \times 35 \times 32$ grid. Both spectra are resolved to 10^{-6} , close to the 10^{-5} precision estimated for $\|\partial \mathbf{u}_{\text{UB}}/\partial t\|$ in table 2. The accuracy of all quantities computed here - equilibria, eigenvalues, eigenfunctions, and transiently turbulent trajectories, is single-precision.

A.3. Arnoldi iteration evaluation of eigenvalues and eigenvectors

The least stable eigenvalues and eigenfunctions of the nontrivial plane Couette flow equilibria can be computed efficiently with Arnoldi iteration. Arnoldi iteration determines the eigenvalues of a matrix A through repeated evaluation of products Aq for test vectors q . In application to plane Couette flow, we use Arnoldi iteration to find the eigenvalues Λ of the linearized time- T map $Df^T|_{a_{\text{EQ}}}$ through repeated computation of $Df^T|_{a_{\text{EQ}}}\delta a$ via a CFD algorithm. As a power method, Arnoldi iteration converges most quickly on the eigenvalues of the largest magnitude, *i.e.*, the most unstable eigenvalues of the map (the least contracting in case of an attractor, such as \mathbf{u}_{LM} for plane Couette flow). At moderate Re the Navier-Stokes dynamics is strongly contracting, with an infinity of stable eigenvalues, $|\Lambda| \ll 1$, and a handful of weakly unstable eigenvalues, $1 < |\Lambda| \sim O(1)$.

The eigenvalues λ of the equilibrium stability matrix $DF|_{a_{\text{EQ}}}$ are related to the eigenvalues Λ of the map $Df^T|_{a_{\text{EQ}}}$ by $\Lambda = e^{\lambda T}$ and the inverse relations $\mu = (1/T) \ln |\Lambda|$ and $\omega = (1/T)(\arg \Lambda + 2\pi n)$. The complex logarithm is multivalued, so the proper value of n must be determined by a secondary calculation, either recomputing Arnoldi with a different T , or examining the rate of oscillation of the eigenfunction integrated by CFD.

As in (A 3), we approximate the linearized map $Df^T|_{a_{\text{EQ}}}\delta a$ with finite differencing and a CFD algorithm:

$$[Df^T|_{a_{\text{EQ}}}\delta a]_m = \frac{1}{\epsilon} (f_{\text{CFD}}^T(\mathbf{u}_{\text{EQ}} + \epsilon \delta \mathbf{u}) - f_{\text{CFD}}^T(\mathbf{u}_{\text{EQ}}), \Phi_m) + O(\epsilon) \quad (\text{A } 5)$$

for $\delta \mathbf{u} = \sum_{n=1}^d \delta a_n \Phi_n$. A choice of $\epsilon = 1e^{-7}$ provides a good balance between maximizing the accuracy of the finite-difference approximation and preserving significant digits through the difference. If greater precision is needed, the linear map may be computed without finite-differencing errors by linearizing the CFD algorithm.

For equilibria Newton searches of § 5, the Arnoldi iteration was initiated with vector δa with random components scaled to roughly match those of a_{EQ} in magnitude. The time parameter in the map was empirically set to $T = 10$.

The resulting unstable eigenvalues, and a set of the least contracting stable ones, are shown in Figure 7. Eigenfunctions \mathbf{v}_{EQ} of linearized Navier-Stokes flow are computed from the eigenvectors b of the finite-time map. The 20 leading eigenfunctions for each equilibrium are available upon request on Channelflow.org; a typical representative pair is plotted (8). Tables 3 and 4 list the numerical values of sets of least unstable eigenvalues of the \mathbf{u}_{LM} , \mathbf{u}_{LB} , \mathbf{u}_{NB} , and \mathbf{u}_{UB} equilibria, together with their symmetries.

						n	$\mu_{\text{LB}}^{(n)}$	$\omega_{\text{LB}}^{(n)}$	$s_1 s_2 s_3$
				Arnoldi $\lambda_{\text{LM}}^{(n)}$	Analytic $\lambda_{\text{LM}}^{(n)}$				
1,2	H	1	0	-0.00616850	-0.00616850	1	0.0501205		S S S
3,4	H	1	1	-0.02179322	-0.02179350	2	1.878e-06		- - -
5,6	H	2	0	-0.02467398	-0.02467401	3	-1.625e-06		- - -
7,8	S	1	1	-0.02916371	-0.02916371	4	-0.0020054		A S A
9,10	H	2	1	-0.04029896	-0.04029901	5	-0.0065977		A A S
11,12	H	3	0	-0.05551652	-0.05551653	6	-0.0069308		S A A
						7	-0.0097953		S A A
						8	-0.0135925		A S A
						9	-0.0239353		S S S
						10	-0.0335130		S S S
						11	-0.0370295		S A A
						12,13	-0.0454857	0.0190660	A A S
						14,15	-0.0484668	0.1025150	S S S
						16,17	-0.0518223	0.0260556	S A A
						18	-0.0554185		A S S
						19,20	-0.0624099	0.0311804	S S S

TABLE 3. (left) Least stable eigenvalues of laminar \mathbf{u}_{LM} equilibrium computed by Arnoldi iteration, compared to the analytic formulae for Stokes (S) and heat-equation (H) modes. (right) \mathbf{u}_{LB} equilibrium stability eigenvalues and symmetries (3.11) of corresponding eigenvectors.

n	$\mu_{\text{NB}}^{(n)}$	$\omega_{\text{NB}}^{(n)}$	$s_1 s_2 s_3$	n	$\mu_{\text{UB}}^{(n)}$	$\omega_{\text{UB}}^{(n)}$	$s_1 s_2 s_3$
1	0.0306497		A S A	1	0.0555837		A A S
2,3	0.0261952	0.056377	S S S	2,3	0.0325292	0.107043	S S S
4	0.0183668		S S S	4,5	0.0160591	0.039238	S A A
5	0.0174064		S A A	6,7	0.0152926	0.284177	S A A
6	0.0158648		A A S	8	0.0106036		A S A
7	-1.047e-07		- - -	9	1.032e-06		- - -
8	-4.709e-07		- - -	10	1.599e-07		- - -
9	-0.0045203		A S A	11,12	-0.0141215	0.057748	S S S
10	-0.0048642		S A A	13	-0.0181827		S A A
11,12	-0.0081398	0.254740	S S S	14,15	-0.0209193	0.173592	A A S
13,14	-0.0151787	0.280906	A A S	16,17	-0.0242951	0.147947	S S S
15,16	-0.0195815	0.308480	S A A	18,19	-0.0264681	0.312192	A S A
17	-0.0233405		A A S	20,21	-0.0274125	0.147147	A A S
18,19	-0.0280165	0.277391	A S A				
20	-0.0359781		S S S				

TABLE 4. Stability eigenvalues and symmetries (3.11) of corresponding eigenvectors: (left) \mathbf{u}_{NB} , (right) \mathbf{u}_{UB} equilibrium.

Appendix B. Tabulation of numerical results

In plane Couette flow simulations infinite x and z directions are replaced with a periodic cell of lengths $[L_x, L_z]$. Cell sizes are also sometimes defined in terms of cell wavenumbers $\alpha = 2\pi/L_x$ and $\gamma = 2\pi/L_z$. Due to the lack of structural stability precise cell size needs to be stated, even for cell sizes as close as $7/4 = 2/1.142857\dots \neq 2/1.14$. The invariant solutions differ not only quantitatively, on % accuracy level, but also qualitatively, and potentially dramatically so - a chaotic dynamical system can undergo an infinity of

bifurcations in a small parameter window. Further important detail that can make it difficult to compare numerical results (but is mostly glossed over in the literature) is the external pressure condition on the flow. In our calculations the spatial mean of the pressure gradient is kept at zero at every instant in time, with no pressure drop across the length of the cell.

Tables 3 and 4 list sets of the least stable linear stability eigenvalues of the \mathbf{u}_{LM} , \mathbf{u}_{LB} , \mathbf{u}_{NB} , and \mathbf{u}_{UB} , together with symmetries of corresponding eigenfunctions. The unstable eigenvalues together with a set of the least contracting stable ones are also shown in Figure 7.

All numerical results tabulated in this section are computed for plane Couette flow with $Re = 400$, $[L_x, L_y, L_z] = [2\pi/1.14, 2, 4\pi/5]$ cell.

REFERENCES

- ANDERSON, E., BAI, Z., BISCHOF, C., BLACKFORD, S., DEMMEL, J., DONGARRA, J., DU CROZ, J., GREENBAUM, A., HAMMARLING, S., MCKENNEY, A. & SORENSEN, D. 1999 *LAPACK Users' Guide*, 3rd edn. Philadelphia, PA: Society for Industrial and Applied Mathematics.
- AUBRY, N., HOLMES, P., LUMLEY, J. L. & STONE, E. 1988 The dynamics of coherent structures in the wall region of turbulent boundary layer. *J. Fluid Mech.* **192**, 115–173.
- BARENGHI, C. 2004 Turbulent transition for fluids. *Physics World* **17** (12).
- BECH, K. H., TILLMARK, N., ALFREDSSON, P. H. & ANDERSSON, H. I. 1995 An investigation of turbulent plane Couette flow at low Reynolds numbers. *J. Fluid Mech.* **286**, 291–325.
- BOTTIN, S., DAVIAUD, F., MANNEVILLE, P. & DAUCHOT, O. 1998 Discontinuous transition to spatiotemporal intermittency in plane Couette flow. *Europhys. Lett.* **43**, 171–176.
- BUSSE, F. H. 2004 Visualizing the dynamics of the onset of turbulence. *Science* **305**, 1574–1575.
- CANUTO, C., HUSSAINI, M. Y., QUATERONI, A. & ZHANG, T. A. 1988 *Spectral Methods in Fluid Dynamics*. Springer-Verlag.
- CANUTO, C., HUSSAINI, M. Y., QUATERONI, A. & ZHANG, T. A. 2006 *Spectral Methods: Fundamentals in Single Domains*. Springer-Verlag.
- CVITANOVIĆ, P., ARTUSO, R., MAINIERI, R., TANNER, G. & VATTAY, G. 2006 *Chaos: Classical and Quantum*. Copenhagen: Niels Bohr Institute, ChaosBook.org.
- CVITANOVIĆ, P., DAVIDCHACK, R. L. & SIMINOS, E. 2007 Relative periodic orbits in Kuramoto-Sivashinsky equation. In preparation.
- DAUCHOT, O. & DAVIAUD, F. 1995 Finite-amplitude perturbation and spots growth mechanism in plane Couette flow. *Phys. Fluids* **7**, 335–343.
- DAUCHOT, O., DAVIAUD, F. & MANNEVILLE, P. 1998 Experimental evidence of streamwise vortices as finite amplitude solutions in transitional plane Couette flow. *Phys. Fluids* **10**, 2597–2607.
- DAUCHOT, O. & VIOUJARD, N. 2000 Phase space analysis of a dynamical model for the subcritical transition to turbulence in plane Couette flow. *European Physical J. B* **14**, 377–381.
- DAVIAUD, F., HEGSETH, J. & BERGE, P. 1992 Subcritical transition to turbulence in plane Couette flow. *Phys. Rev. Lett.* **69**, 2511–2514.
- VAN DOORNE, C. W. H. 2004 Stereoscopic PIV on transition in pipe flow. PhD thesis, Delft.
- DRAZIN, P. & REID, W. H. 1981 *Hydrodynamic Stability*. Cambridge: Cambridge University Press.
- EATON, J. 2007 GNU Octave: a high-level language for numerical computation. *Tech. Rep.*. University of Wisconsin.
- FAISST, H. & ECKHARDT, B. 2003 Traveling waves in pipe flow. *Physical Review Letters* **91**, 224502.
- FOIAS, C., NICOLAENKO, B., SELL, G. R. & TEMAM, R. 1985 Inertial manifold for the Kuramoto-Sivashinsky equation. *C. R. Acad. Sci. I-Math* **301**, 285–288.
- FRIGO, M. & JOHNSON, S. 2005 The design and implementation of FFTW3. *Proceedings of the IEEE* **93** (2), 216–231, special issue on “Program Generation, Optimization, and Platform Adaptation”.

- GIBSON, J. F. 2002 Dynamical systems models of wall-bounded, shear-flow turbulence. PhD thesis, Cornell University.
- GIBSON, J. F. 2007 Channelflow: a spectral Navier-Stokes simulator in C++. *Tech. Rep.*. Georgia Institute of Technology, open-source Navier-Stokes code.
- HAMILTON, J. M., KIM, J. & WALEFFE, F. 1995 Regeneration mechanisms of near-wall turbulence structures. *Journal of Fluid Mechanics* **287**, 317–348.
- HEGSETH, J., DAVIAUD, F. & BERGE, P. 1992 Intermittent turbulence in plane and circular Couette flow. In *Ordered and Turbulent Patterns in Taylor-Couette Flow* (ed. C. D. Andereck & F. Hayot), pp. 159–166. New York: Plenum Press.
- HOF, B., VAN DOORNE, C. W. H., WESTERWHEEL, J., NIEUWSTADT, F. T. M., FAISST, H., ECKHARDT, B., WEDIN, H., KERSWELL, R. R. & WALEFFE, F. 2004 Experimental observation of nonlinear traveling waves in turbulent pipe flow. *Science* **305** (5690), 1594–1598.
- HOF, B., JUEL, A. & MULLIN, T. 2003 Scaling of the turbulence transition threshold in a pipe. *Phys. Rev. Lett.* **91**, 244502.
- HOLMES, P., LUMLEY, J. L. & BERKOOZ, G. 1996 *Turbulence, Coherent Structures, Dynamical Systems and Symmetry*. Cambridge: Cambridge University Press.
- HOPF, E. 1948 A mathematical example displaying features of turbulence. *Comm. Appl. Math.* **1**, 303–322.
- JIMÉNEZ, J., KAWAHARA, G., SIMENS, M. P., NAGATA, M. & SHIBA, M. 2005 Characterization of near-wall turbulence in terms of equilibrium and bursting solutions. *Phys. Fluids* **17**, 015105.
- KAWAHARA, G. & KIDA, S. 2001 Periodic motion embedded in Plane Couette turbulence: regeneration cycle and burst. *Journal of Fluid Mechanics* **449**, 291–300.
- KEVREKIDIS, I. G., NICOLAENKO, B. & SCOVEL, J. C. 1990 Back in the saddle again: a computer assisted study of the Kuramoto-Sivashinsky equation. *Siam J. Appl. Math.* **50**, 760–790.
- KIM, J., MOIN, P. & MOSER, R. 1987 Turbulence statistics in fully developed channel flow at low Reynolds number. *Journal of Fluid Mechanics* **177**, 133–166.
- KLEISER, L. & SCHUMAN, U. 1980 Treatment of incompressibility and boundary conditions in 3-D numerical spectral simulations of plane channel flows. In *Proc. 3rd GAMM Conf. Numerical Methods in Fluid Mechanics* (ed. E. Hirschel), pp. 165–173. GAMM, Viewweg, Braunschweig.
- LÓPEZ, V., BOYLAND, P., HEATH, M. T. & MOSER, R. D. 2006 Relative periodic solutions of the complex ginzburg–landau equation. *SIAM Journal on Applied Dynamical Systems* **4** (4), 1042–1075.
- LUNDBLADH, A. & JOHANSSON, A. 1991 Direct simulation of turbulent spots in plane Couette flow. *J. Fluid Mech.* **229**, 499–516.
- MALERUD, S., MALFY, K. J. & GOLDBURG, W. I. 1995 Measurements of turbulent velocity fluctuations in a planar Couette cell. *Phys. Fluids* **7**, 1949–1955.
- MANNEVILLE, P. 2004 Spots and turbulent domains in a model of transitional plane Couette flow. *Theoretical and Computational Fluid Dynamics* **18**, 169–181.
- MOEHLIS, J., ECKHARDT, B. & FAISST, H. 2004a Fractal lifetimes in the transition to turbulence. *CHAOS* **14**, S11.
- MOEHLIS, J., FAISST, H. & ECKHARDT, B. 2004b A low-dimensional model for turbulent shear flows. *New Journal of Physics* **6**, 56.
- MOEHLIS, J., FAISST, H. & ECKHARDT, B. 2004c Periodic orbits and chaotic sets in a low-dimensional model for shear flows. *SIAM J. Applied Dynam. Systems* **4**, 352–376.
- MOSER, R., MOIN, P. & LEONARD, A. 1983 A spectral method for the Navier-Stokes equations with applications to Taylor-Couette flow. *J. Comp. Phys.* **52**, 524–544.
- NAGATA, M. 1990 Three-dimensional finite-amplitude solutions in plane Couette flow: bifurcation from infinity. *J. Fluid Mech.* **217**, 519–527.
- PEYRET, R. 2002 *Spectral Methods for Incompressible Flows*. Springer-Verlag.
- ROMANOV, V. A. 1973 Stability of plane-parallel Couette flow. *Functional Anal. Applics.* **7**, 137–146.
- SCHMIEGEL, A. 1999 Transition to turbulence in linearly stable shear flows. PhD thesis, Philipps-Universität Marburg.

- SCHMIEGEL, A. & ECKHARDT, B. 1997 Fractal stability border in plane Couette flow. *Phys. Rev. Lett.* **79**, 5250.
- SIROVICH, L. & ZHOU, X. 1994 Reply to “Observations regarding ‘Coherence and chaos in a model of turbulent boundary layer’ by X. Zhou and L. Sirovich”. *Phys. Fluids* **6** (4), 1579–1582.
- SKUFCA, J. D. 2005 Understanding the chaotic saddle with focus on a 9-variable model of planar covette flow. PhD thesis, U. Maryland.
- SKUFCA, J. D., YORKE, J. A. & ECKHARDT, B. 2006 Edge of chaos in a parallel shear flow. *Phys. Rev. Lett.* **96** (17), 174101.
- SMITH, T. R., MOEHLIS, J. & HOLMES, P. 2005 Low-dimensional models for turbulent plane couette flow in a minimal flow unit. *J. Fluid Mech.* **538**, 71–110.
- SPALART, P. R., MOSER, R. D. & ROGERS, M. M. 1990 Spectral methods for the Navier-Stokes equations with one infinite and two periodic directions. *J. Comp. Physics* **96**, 297–324.
- TILLMARK, N. 1995 On the spreading mechanisms of a turbulent spot in plane Couette flow. *Europhys. Lett.* **32**, 481–485.
- TILLMARK, N. & ALFREDSSON, P. H. 1992 Experiments on transition in plane Couette flow. *J. Fluid Mech.* **235**, 89–102.
- TREFETHEN, L. N. 2000 *Spectral Methods in Matlab*. Philadelphia: SIAM.
- TREFETHEN, L. N. & BAU, D. 1997 *Numerical Linear Algebra*. SIAM.
- VISWANATH, D. 2007a The dynamics of transition to turbulence in plane Couette flow. Unpublished, arXiv:/physics/0701337.
- VISWANATH, D. 2007b Recurrent motions within plane Couette turbulence. *J. Fluid Mech.* **580**, 339–358, arXiv:/physics/0604062.
- WALEFFE, F. 1995 Hydrodynamic stability and turbulence: beyond transients to a self-sustaining process. *Stud. Applied Math.* **95**, 319–343.
- WALEFFE, F. 1997 On a self-sustaining process in shear flows. *Physics of Fluids* **9**, 883–900.
- WALEFFE, F. 1998 Three-dimensional coherent states in plane shear flows. *Physical Review Letters* **81**, 4140–4143.
- WALEFFE, F. 2001 Exact coherent structures in channel flow. *Journal of Fluid Mechanics* **435**, 93–102.
- WALEFFE, F. 2003 Homotopy of exact coherent structures in plane shear flows. *Physics of Fluids* **15**, 1517–1543.
- WALEFFE, F. & WANG, J. 2005 Transition threshold and the self-sustaining process. In *Non-uniqueness of Solutions to the Navier-Stokes Equations and their Connection with Laminar-Turbulent Transition* (ed. T. Mullin & R. R. Kerswell), pp. 85–106. Kluwer.
- WANG, J., GIBSON, J. F. & WALEFFE, F. 2007 Lower branch coherent states in shear flows: transition and control. *Phys. Rev. Lett.* **98** (20).
- WEDIN, H. & KERSWELL, R. R. 2004 Exact coherent structures in pipe flow: travelling wave solutions. *Journal of Fluid Mechanics* **508**, 333–371.
- ZHOU, X. & SIROVICH, L. 1992 Coherence and chaos in a model of turbulent boundary layer. *Phys. Fluids A* **4**, 2855–2874.